Construction and Building Materials 222 (2019) 458–473

Contents lists available at ScienceDirect

Construction and Building Materials

journal homepage: www.elsevier.com/locate/conbuildmat

Fiber-reinforced internally unstable soil against suffusion failure

Kuo-Hsin Yang [a,*], Shao-Bang Wei [b], Williams Mathieu Adilehou [b], Hao-Che Ho [a]

[a] Department of Civil Engineering, National Taiwan University (NTU), 1, Sec. 4, Roosevelt Rd., Taipei 106, Taiwan
[b] Department of Civil and Construction Engineering, National Taiwan University of Science and Technology (Taiwan Tech), 43, Sec. 4, Keelung Rd., Taipei 106, Taiwan

HIGHLIGHTS

- Investigation on the hydraulic responses of fiber-reinforced gap-graded soil.
- Evaluation of the effectiveness of fibers to enhance the soil erosion resistance.
- Examination of soil-fiber interactions and improvement mechanism against suffusion.
- Assessment of the influence of fiber parameters on the behavior of fiber-reinforced soil.
- Identification of the failure mode transformation with an increasing number of fibers.

ARTICLE INFO

Article history:
Received 2 January 2019
Received in revised form 13 June 2019
Accepted 17 June 2019

Keywords:
Fiber-reinforced sand
Internal stability
Hydraulic failure
Erosion
Suffusion

ABSTRACT

Gap-graded soil, classified as internally unstable soil, is susceptible to hydraulic failure due to the migration and erosion of fine particles through the coarse particle matrix at a relatively low hydraulic gradient. This internal erosion process, known as suffusion, is a hazardous phenomenon that can undermine the strength and stability of earth structures or their foundation. In this study, a series of seepage tests was conducted to investigate the hydraulic responses of fiber-reinforced gap-graded soil (FRS) and to evaluate the effectiveness of adding fiber to improve the internal erosion resistance of soil against suffusion. The respective influences of fiber parameters (i.e., fiber content and length) on the failure mode, hydraulic conductivity (k), Forchheimer coefficients (κ and β), and critical hydraulic gradient (i_{cr}) of FRS were quantitatively assessed. Soil-fiber interactions and improvement mechanisms, including fiber netting effect and vertical reinforcing effect, are discussed. Experimental results demonstrated that the inclusion of a small number of fibers can effectively improve the internal erosion resistance of gap-graded soils against suffusion. Hydraulic conductivity decreases and the Forchheimer coefficient β increases as fiber content increases. With an increase in the total number of fibers (i.e., high fiber content and short fiber length), the critical hydraulic gradient increases at various stages of the erosion process (determined at the onset of internal erosion, at the transition of flow from laminar to turbulent conditions, and at hydraulic failure). When the normalized number of fibers exceeds 1%, the failure mode shifts from suffusion to general piping, which resembles the failure mode of internally stable soil (i.e., uniform soil).

1. Introduction

Internal erosion of soil is a process during which soil particles are forced to migrate along with seepage flow. This process presents hazards in geotechnical engineering and can undermine the integrity, strength, and stability of earth structures such as dams, embankments, and their foundations [33,39,41,42,78,98,104]. Foster et al. [36] statistically analyzed dam failure cases compiled from the International Commission of Large Dams (ICOLD) and found 46.1% of failure cases to be associated with internal erosion. Richards and Reddy [84] reported that up to 50% of dams worldwide are at risk of internal erosion. Danka and Zhang [19] noted that the failure rate of dikes, man-made dams, and landslide dams due to internal erosion are 14%, 37%, and 8%, respectively. The increasing hazards of soil piping and internal erosion have gained considerable attention given rising flood levels and increasing rainfall intensity following global warming and extreme weather [19,80,82,83]. Consequently, mitigating seepage-induced adverse impacts and enhancing the stability of earth structures represent an urgent and challenging task.

* Corresponding author.
E-mail address: khyang@ntu.edu.tw (K.-H. Yang).

https://doi.org/10.1016/j.conbuildmat.2019.06.142
0950-0618/

Notations

Basic SI units are given in parentheses

A	parameter for fiber orientation model (dimensionless)
B	parameter for fiber orientation model (dimensionless)
b	distance to the center of the reference sphere (m)
C_u	uniformity coefficient (dimensionless)
C_c	coefficient of curvature (dimensionless)
D_r	relative density (%)
d_{10}	effective particle size (m)
d_{50}	mean particle size (m)
d_f	fiber diameter (m)
d_{15c}	particle size at finer percent of 15% in coarse fraction (m)
d_{85f}	particle size at finer percent of 85% in fine fraction (m)
e_{max}	maximum void ratio (dimensionless)
e_{min}	Minimum void ratio (dimensionless)
F	finer percent at particle diameter d (%)
G_s	specific gravity of soil (dimensionless)
G_{sf}	specific gravity of fiber (dimensionless)
H	finer percent increment between d and $4d$ (%)
Δh	differential hydraulic head (m)
i	hydraulic gradient (dimensionless)
i_{cr}	critical hydraulic gradient (dimensionless)
$i_{cr,\ onset}$	i_{cr} at the onset of internal erosion (dimensionless)
$i_{cr,\ interest}$	i_{cr} at the transition of flow condition (dimensionless)
$i_{cr,\ failure}$	i_{cr} at the hydraulic failure (dimensionless)
k	hydraulic conductivity (m/s)
L	distance between the two measuring valves (m)
L_f	fiber length (m)
l_1, l_2	length and width of the cut plane (m)
N_f	normalized number of fibers (dimensionless)
N^H	number of fiber in the horizontal plane
N^V	number of fiber in the vertical plane
n	parameter for fiber orientation model (dimensionless)
R	radius of the reference sphere for fiber orientation analysis (m)
R_e	Reynolds number (dimensionless)
V_{1f}	volume of a single fiber (m^3)
V_s	volume of the reference sphere for fiber orientation analysis (m^3)
v	discharge velocity (m/s)
α	fiber orientation on horizontal plane (degree)
β	Forchheimer coefficient (1/m)
$\gamma_{d,\max}$	maximum dry unit weight (kN/m^3)
$\gamma_{d,\min}$	minimum dry unit weight (kN/m^3)
κ	Forchheimer coefficient (m^2)
θ	fiber orientation on vertical plane (degree)
ρ_f	volumetric fiber content (%)
ω_f	gravimetric fiber content (%)

Fry [37] and Fell and Fry [32] have classified soil internal erosion into four failure modes: backward erosion (i.e., general piping), suffusion (i.e., segregation piping), contact erosion, and concentrated leak erosion. This study focuses on the second failure mode, suffusion, which involves the migration of fine particles through the matrix of coarse particles driven by seepage force. Fine-particle loss due to suffusion can compromise soil stability by bringing down stress chains and impose risks to whole earth structures.

Gap-graded soils are often used as shell materials in embankment dams. Materials for the core are supposed to be widely graded but a widely graded soil may become gap graded as a result of particle segregation during construction [32,33,70,103]. As a result, suffusion could occur in the shell, core or filter of earth-filled embankments, especially those constructed using broadly graded or gap-graded soils [54]. Chang and Zhang [13] stated that suffusion can occur in gap-graded soil with a fine fraction of less than 35% and in broadly graded soil with a fine fraction no greater than 20%. Skempton and Brogan [90] conducted a series of upward seepage tests on sandy gravel and found that suffusion can occur at a relatively low critical hydraulic gradient, between approximately one fifth and one-third of the theoretical value suggested by Terzaghi [94].

Soil hydraulic failure modes are governed by the internal stability of soil and hydromechanical conditions (i.e., soil stress, seepage direction, and hydraulic gradient) [1,2,10,12,52–54,72,73,90,91]. The term *internal stability* refers to the ability of the coarse fraction of soil to prevent loss of its fine fraction due to seepage flow. Various empirical criteria have been developed to evaluate the potential internal stability of soil [11,13,46,47,56,54,55,63,64,67,97]. Soil that is classified as internally unstable (i.e., gap-graded and broadly graded with a certain fine fraction) is susceptible to suffusion, whereas soil classified as internally stable (i.e., uniform) tends to exhibit piping-type failure.

Fiber reinforcement is a technique whereby randomly distributed natural or synthetic fibers are mixed uniformly with soil to improve the mechanical and hydraulic performance of soil in geotechnical and geoenvironmental applications. Fiber reinforcement has proven to be a promising technique for projects involving stabilizing thin soil veneers, repairing locally failed slopes, improving the bearing capacity of soft ground, strengthening soil in footings, pavement, and earth retaining walls, increasing dynamic resistance to liquefaction, mitigating desiccation cracking of compacted clay systems, enhancing soil piping resistance in hydraulic structures, and reducing surficial soil erosion [15,44,50,60,65,71,79,86,87,93,96,100,101,105]. Hejazi et al. [43] provide a review of the applications and benefits of soil reinforcement using natural and synthetic fibers.

Previous studies have demonstrated the benefits of mixing fibers with soil in enhancing the mechanical behavior of soil. The key parameters evaluated in these studies are soil type, fiber type, length, and content, as well as cement content and compaction conditions. When soil is subjected to compressive or shear loadings, inclusion of fibers in soil can remarkably enhance soil peak shear strength, and reduce the loss of postpeak shear strength [3–5,14,23,24,40,48,51,58,69,75,85,95,105]. When soil is subjected to tensile loadings or flexural distress induced by differential settlement, fiber reinforcement can increase soil tensile strength and flexural rigidity [17,34,49,61,76,92]. In the presence of fibers, soil stiffness tends to decrease and soil changes from brittle to ductile deformation characteristics under both monotonic and cycle loadings [59,60].

Regarding the improvement of soil hydraulic performance, experimental tests on fiber-reinforced soil subjected to seepage have been reported in the literature [4,20–22,26,27,29,28,38,66,89,99]. The primary focuses of these studies are on the effect of fiber parameters (i.e., fiber type, length, and content) and soil fine content on the hydraulic conductivity and critical hydraulic gradient (i.e., piping resistance) of soil. These studies have found that fiber reinforcement can effectively reduce the soil permeability and enhance the soil piping resistance by deferring the occurrence of soil piping at a high hydraulic gradient. Akay et al. [4] found a threshold for the influence of fiber content on the hydraulic conductivity of uniform sand with a few fines. Their experimental results indicated the saturated hydraulic conductivity changed slightly for the fiber content ranged from 0.0% to 0.5%, but it

decreased as the fiber content increased from 0.5% to 1.0%. In addition, the effect of soil relative density on the hydraulic response of fiber-reinforced uniform sand was evaluated by Yang et al. [99]. The test specimens were prepared at two different target relative density, D_r = 50% and 70%, to represent loose and dense soil conditions. The test results revealed that the fiber has a greater effect in the dense specimen than in the loose specimen. At a given fiber length and content, the hydraulic performance in enhancing the soil piping resistance and reducing the seepage velocity was more pronounced in the dense specimen. The superior performance in the dense specimen results from increased soil-fiber interaction in dense soil states and less pore space which could be easily blocked or filled with a given amount of fibers. Estabragh et al. [29] reported similar findings that the critical hydraulic gradient of fiber-reinforced silty sand increased as the void ratio of the test specimen decreased.

Model tests and numerical analyses of fiber-reinforced embankments under rainfall and seepage conditions were also performed [4–6,39,100]. These studies highlighted that the use of fiber-reinforced soil as backfill possessed the combined merits of improvement in both mechanical and hydraulic performance of soil. These studies demonstrated that the fiber reinforcement can be considered as a viable alternative to enhance the hydraulic performance of earth structures by delaying the advance of seepage, reducing soil piping potential, improving system slope stability against seepage, and thus preventing the hydraulic failure of earth structures.

The aforementioned studies on the hydraulic performance of fiber-reinforced soil have focused on the reinforcing effect of fibers on internally stable soil in which general piping is the predominant failure mode. The reinforcing effect and improvement mechanism of fibers on internally unstable soil against suffusion failure have not been evaluated yet. Accordingly, this study conducts a series of experimental tests on fiber-reinforced gap-graded soil (FRS) against suffusion. The objectives of this study are as follows: (1) to investigate the hydraulic responses, erosion process, and failure mode of FRS subjected to seepage; (2) to evaluate the influence of fiber parameters (i.e., fiber length and content) on the internal erosion resistance of FRS; and (3) to understand soil-fiber interactions and improve the FRS mechanism against suffusion. The results and discussion in this study provide insight into the application of fiber reinforcement to earth structures backfilled with gap-graded soil that are at risk of soil suffusion.

2. Experimental program

2.1. Seepage test system

A series of seepage tests were conducted to evaluate the effectiveness of adding fiber to improve the internal erosion resistance of soil against suffusion. An upward seepage test system (Fig. 1), consisting of a constant head device, a permeameter, and measuring systems, was developed and complied with ASTM D2434 [7].

The constant head device included an elevated water supply reservoir and a water barrel positioned at a lower elevation. The permeameter was composed of a transparent acrylic cylindrical cell and a bottom pedestal. The transparent cylindrical cell enabled visual observations of seepage and suffusion progress in soil specimens during tests. The pedestal, filled with marbles and covered with porous screens and nonwoven geotextiles, was used to distribute upward seepage evenly across soil specimens (Fig. 1c). Graduated manometers were connected to the permeameter to measure hydraulic head difference (i.e., head loss) at a given distance of the seepage path (Fig. 1a and b). The readers are referred to Yang et al. [99] for detailed description and functions of the seepage test system.

The discharge velocity (v) at a given hydraulic gradient was calculated by dividing the collected discharge volume at a certain time period by the cross-sectional area of the specimen. The corresponding hydraulic gradient (i) was then calculated at each test stage as:

$$i = \frac{\Delta h}{L} \tag{1}$$

where Δh is the hydraulic head difference between two manometers with a distance L (=11 cm).

2.2. Material properties and test program

The gap-graded soil used in the tests was composed of 85% coarse sand and 15% fine sand. Both coarse and fine sands are quartz sand and have sub-angular grain shape. The fine sand, coarse sand, and gap-graded soil were denoted as F, C, and G, respectively. Fig. 2 displays the grain size distribution curves and images of these soils, and Table 1 summarizes the soil properties. The fine sand, coarse sand, and gap-graded soil had respective mean particle sizes (d_{50}) of 0.28, 3.41, and 3.19 mm, and all were classified as poorly graded sand (SP) according to the Unified Soil Classification System (USCS). The minimum and maximum dry unit weights of soil, determined in accordance with ASTM D4253 and D4254, [8,9], were $\gamma_{d,min}$ = 13.73, 15.79, and 17.36 kN/m^3 and $\gamma_{d,max}$ = 16.28, 17.46, and 19.03 kN/m^3 for fine sand, coarse sand, and gap-graded soil, respectively. Based on the seepage test results, the hydraulic conductivity of the fine sand, coarse sand, and gap-graded soil were k = 0.05, 9.88, and 1.2 cm/s, respectively.

The three internal stability criteria [47,54–56] listed in Table 2 were used to assess the internal stability of the tested soils. These three internal stability criteria are widely used in design specifications and by researchers to assess the internal stability of granular soil [11,13,62,90,97]. All criteria listed in Table 2 were developed based on the geometric relationship of soil grain sizes: Istomina's method concerned the soil's coefficient of the uniformity; Kezdi's method is a modified version of Terzaghi's filter criteria [30] based on the ratio of grain size in coarser and finer fractions; and Kenney and Lau's method is based on the shape of a soil's grain size curve. For the test soils, gap-graded soil was classified as transitional by Istomina's method and as internally unstable by Kezdi's and Kenney and Lau's methods, whereas fine and coarse sand were both classified as internally stable by all three criteria. Fig. 3 shows the variation in Kezdi's and Kenney and Lau's criterion indices with the finer percent selected at an arbitrary particle diameter. Some of the criterion index values for gap-graded soil were within the internal unstable zone in Fig. 3a and b.

Polypropylene (PP) fiber was used for the reinforced specimens. PP fiber is the most widely adopted synthetic fiber for soil reinforcement [57,101]. Das and Viswanadham [21] reported that PP fiber performed better than polyester (PET) fiber in increasing seepage resistance. It is because the PET fiber has a specific gravity higher than the PP fiber. For the same fiber content, a larger specific gravity implies a lower fiber volume and a less number of fibers, and hence reduces the benefit of improving the piping resistance of soil. Table 3 summarizes the physical and mechanical properties of the test fibers. The PP fiber tested in this study had a circular cross-section with an average diameter of 0.0577 mm. The specific gravity of the fiber was G_{sf} = 0.91, slightly lower than that of water. Fiber lengths of 6, 12, and 19 mm (Fig. 4) and gravimetric fiber contents of 0%, 0.1%, 0.2%, and 0.3% were used in the tests.

Table 4 lists the seepage test program. A total of 12 seepage tests were conducted involving three unreinforced and nine reinforced soil tests. The tests were numbered by the following rules. The first letter indicates soil type: F, C, G, and R represent fine sand, coarse sand, gap-graded soil, and FRS, respectively. The second and third letters used for FRS denote the gravimetric fiber content and fiber length, respectively. For example, R-0.1–6 indicates the reinforced specimen with a fiber content ω_f = 0.1% and fiber length L_f = 6 mm.

2.3. Specimen preparation and test procedures

Specimens are 10.5 cm in diameter, 13 cm in height and prepared at the target relative density D_r = 70%. The required weight of dry soil for the target relative density was determined using the relative density equation,

$$D_r = \frac{e_{max} - e}{e_{max} - e_{min}} \tag{2}$$

where e_{max}, e_{min}, and e are the maximum, minimum, and target void ratios of soil. The expected weight of fiber for the reinforced specimens was then calculated considering the dry weight of soil. The gravimetric fiber content ω_f was calculated using Eq. (3):

$$\omega_f = \frac{W_f}{W_s} \tag{3}$$

where W_f and W_s are the dry weight of fiber and soil, respectively.

The specimen was carefully prepared to prevent segregation and ensure the uniformity. First, the known soil-fiber quantity was carefully mixed by hand. The soil-fiber mixture was moisturized during hand-mixing to avoid separation. Based on the experience learned from the specimen preparation, a homogeneous sand-fiber mixture can be easily achieved when the fiber content is low (up to 0.3%). Second, after the soil and fiber were thoroughly mixed, the moist soil-fiber mixture was then filled in the permeameter in five layers (2.6 cm thickness per layer). Filling in several small layers was to ensure the uniformity of the soil-fiber mixture through the entire specimen. Each layer was tamped with a metal rod to control

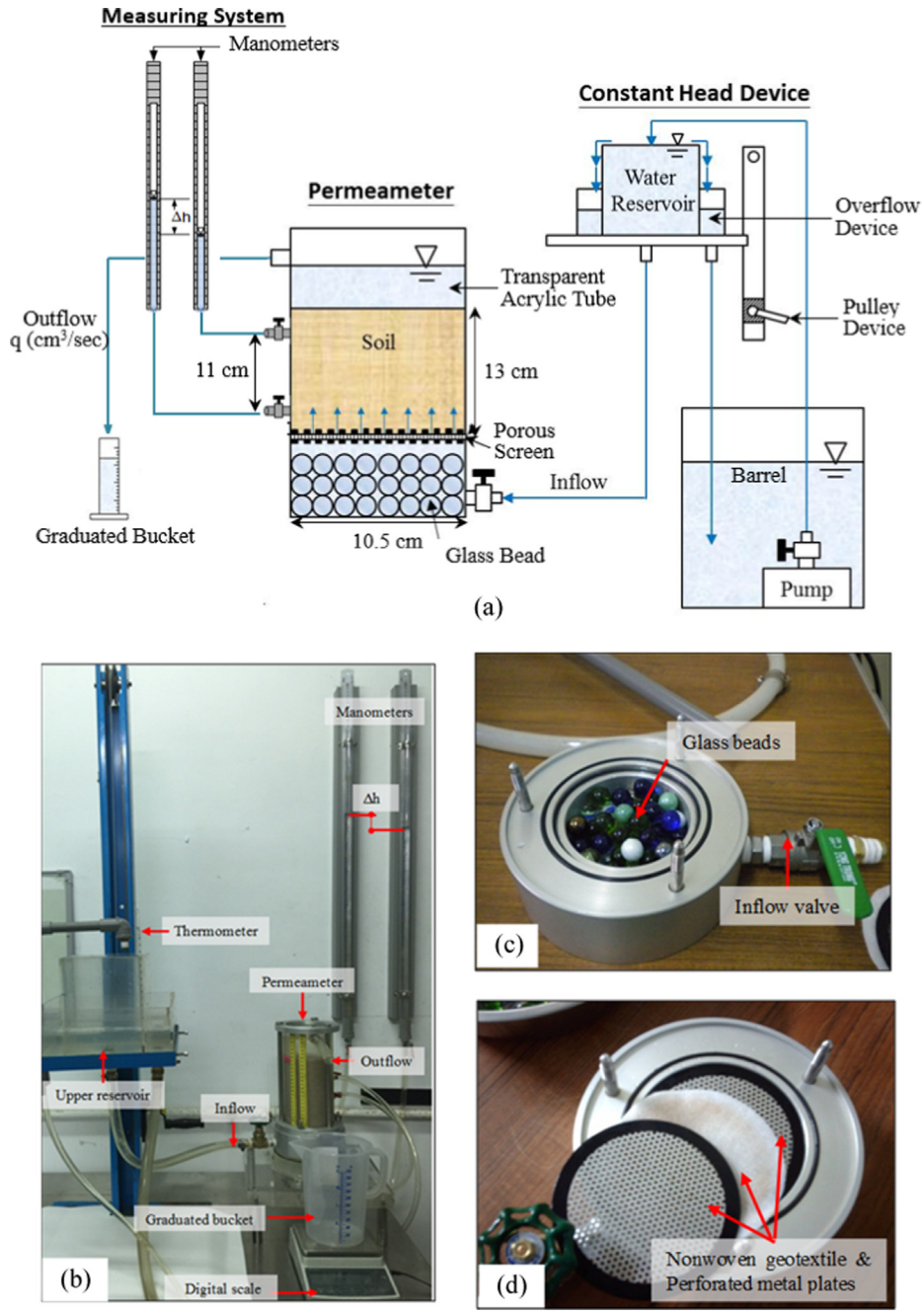

Fig. 1. Test apparatus: (a) illustration; (b) photo; (c) and (d) details of pedestal; (d) nonwoven geotextile and perforated metal plates.

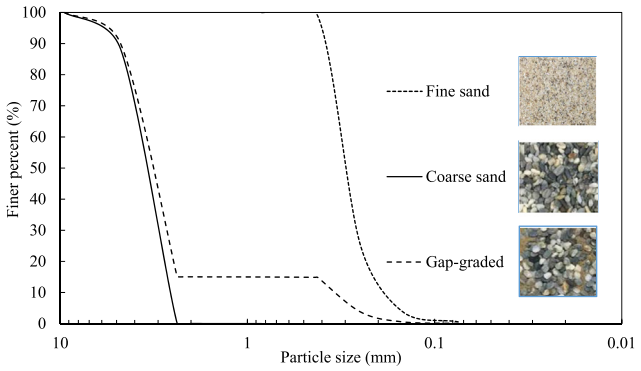

Fig. 2. Grain size distribution curves and photographs of soils.

its height and density. This procedure was repeated until the desired specimen height (=13 cm) was reached. Third, a visual inspection was conducted to ensure uniformity through the specimen. A similar specimen preparation procedure has been adopted by various researchers [18,16,20,29,81,99,102,101].

After specimen preparation, each specimen was submerged in water and subjected to constant seepage flow under a low hydraulic head that did not affect specimen stability for 24 h to ensure full specimen saturation. Afterward, the seepage test began by applying a series of hydraulic heads to the specimen until soil hydraulic failure occurred. The applied hydraulic head was increased at increments of 1.5 cm (approximately $\Delta i = 0.1$) and maintained for at least 15 min until the hydraulic heads in the manometers stabilized, indicating that equilibrium was reached. At each test stage, changes in the hydraulic gradient, discharge velocity, top and side view photographs, and specimen height were measured and recorded. After soil hydraulic failure occurred, the seepage was halted and the thickness of the fine deposits at the top of the specimen was measured. The repeatability and consistency of the test results were verified by conducting the test three times under the same conditions. Fig. 5 depicts a demonstration of test replicability using Test R-0.2-6 as an example.

Table 1
Soil properties and internal stability.

Item	Fine sand (F)	Coarse sand (C)	Gap-graded (G)
Soil properties			
Specific gravity G_s	2.67	2.69	2.69
Effective particle size d_{10} (mm)	0.17	1.69	0.35
Mean particle size d_{50} (mm)	0.28	3.41	3.19
Uniformity coefficient C_u	1.82	2.17	10.02
Coefficient of curvature C_c	1.18	1.4	6.14
Soil classification (USCS)	SP	SP	SP
Maximum dry unit weight $\gamma_{d,max}$ (kN/m^3)	16.28	17.46	19.03
Minimum dry unit weight $\gamma_{d,min}$ (kN/m^3)	13.73	15.79	17.36
Maximum void ratio e_{max}	0.91	0.67	0.52
Minimum void ratio e_{min}	0.61	0.51	0.38
Hydraulic conductivity of soil k (cm/s)	0.05	9.88	1.2
Internal stability criteria			
Istomina [47] C_u	1.82 (Stable)	2.17 (Stable)	10.02 (Transition)
Kezdi [56] $(d_{15c}/d_{85f})_{max}$	1.49 (Stable)	1.49 (Stable)	10 (Unstable)
Kenny and Lau [55] $(H/F)_{min}$	2.65 (Stable)	2.75 (Stable)	0 (Unstable)

Table 2
Summary of soil internal stability criteria.

References	Internal stability criteria
Istomina [47][1]	$C_u \leq 10$, internally stable $10 < C_u < 20$, transitional $C_u \geq 20$, internally unstable
Kezdi [56][2]	$(d_{15c}/d_{85f})_{max} \leq 4$, internally stable
Kenney and Lau [54,55][3]	Original (1985): $(H/F)_{min} > 1.3$, internally stable Modified (1986): $(H/F)_{min} > 1.0$, internally stable

[1] C_u is soil uniformity coefficient obtained from the grain size distribution curve.
[2] d_{15c} is the particle size at finer percent of 15% in coarser fraction and d_{85f} is the particle size at finer percent of 85% in finer fraction.
[3] F is the finer percent at an arbitrary particle diameter d; H is the finer percent increment between d and 4d.

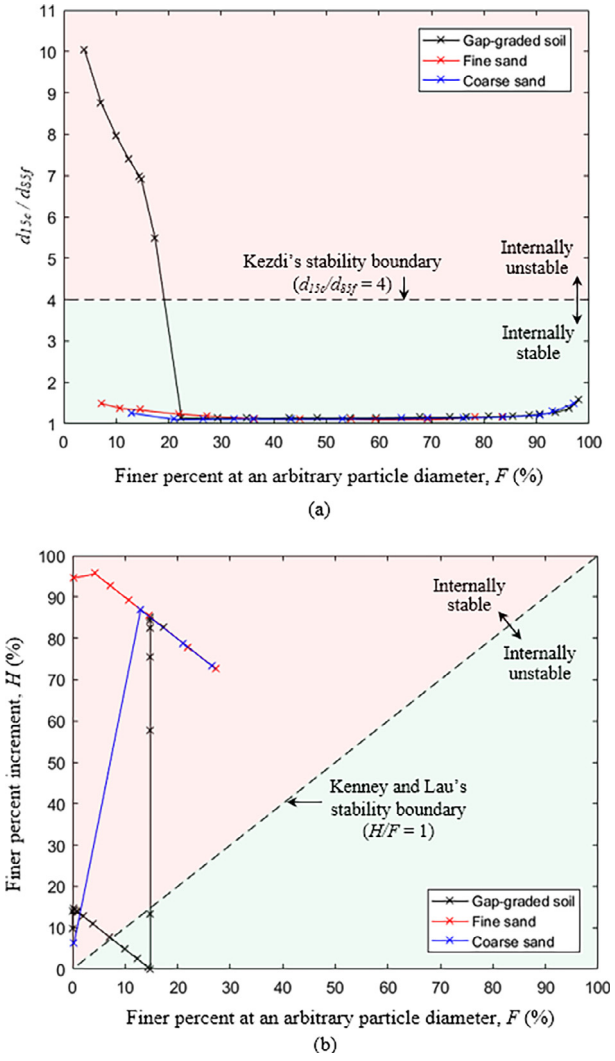

Fig. 3. Evaluation of soil internal stability: (a) Kezdi method; (b) Kenney and Lau method.

3. Soil-fiber interactions and improvement mechanism

Fiber orientation and scanning electron microscope (SEM) analyses were performed to understand the soil-fiber interaction and mechanisms of fiber to improve the internal erosion resistance of soil against suffusion. For fiber orientation analysis, the procedure proposed by Diambra et al. [25] to determine fiber orientation distribution in reinforced sand samples was adopted. In the fiber orientation analysis, a generalized fiber orientation distribution function ρ(θ), representing the volumetric fiber content within an infinitesimal volume with an orientation angle of θ on the vertical plane, is expressed as follows [68]:

$$\rho(\theta) = \bar{\rho}(A + B|\cos^n\theta|) \tag{4}$$

where $\bar{\rho}$ is the average volumetric fiber content of the soil-fiber sample; A, B, and n are fiber orientation parameters that can be calibrated from the measured number of fibers intersecting a given area on a plane of the soil-fiber sample. The correlation of A, B and n are:

$$B = \frac{1 - A}{\int_0^{\pi/2} \cos^{n+1}(\theta) d\theta} \tag{5}$$

The probability density function $f(\theta)$ of the fiber orientation is defined as:

Table 3
Fiber properties and test conditions.

Item	Value
Fiber properties	
Type	Polypropylene (PP) fiber
Cross-section shape	Circular
Diameter d_f (mm)	0.0557
Specific gravity G_{sf}	0.91
Denier (g/9000 m)	20
Ultimate tensile strength (MPa)	250
Melting point (°C)	160–170
Water absorption	No
Test conditions	
Fiber content ω_f (%)	0, 0.1, 0.2, 0.3
Length L_f (mm)	6, 12, 19

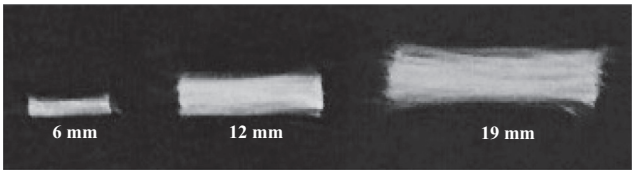

Fig. 4. Fibers with different lengths.

Table 4
Summary of test results.

Test	Fiber variables			Measured hydraulic response				Forchheimer coefficient		Reynolds number
	ω_f (%)	L_f (mm)	N_f (%)	$i_{cr,onset}$	$i_{cr,intersect}$	$i_{cr,failure}$	k (cm/s)	κ (10^{-6} cm^2)	β (l/cm)	Re at $i_{cr,\ intersect}$
F	0	0	0	–	–	1.01	0.05	–	–	–
C	0	0	0	–	–	–	9.88	–	–	–
G	0	0	0	0.18	0.19	0.27	1.2	11	−540	9.3
R-0.1-6	0.1	6	0.69	0.32	0.41	1.67	0.72	6.4	940	10.5
R-0.2-6	0.2	6	1.39	0.55	0.67	1.99	0.5	4.3	2034	10.1
R-0.3-6	0.3	6	2.08	0.71	0.73	2.36	0.38	3.6	2963	7.6
R-0.1-12	0.1	12	0.35	0.27	0.35	0.95	0.97	8.3	−89	13.7
R-0.2-12	0.2	12	0.69	0.37	0.45	2.15	0.77	6.7	1053	11.4
R-0.3-12	0.3	12	1.04	0.43	0.54	2.57	0.6	5.2	1807	10.4
R-0.1-19	0.1	19	0.22	0.21	0.30	0.7	1.08	9.4	−247	12.7
R-0.2-19	0.2	19	0.44	0.29	0.40	1.57	0.89	8.3	469	11
R-0.3-19	0.3	19	0.66	0.33	0.48	2.28	0.71	6.0	1758	9.9

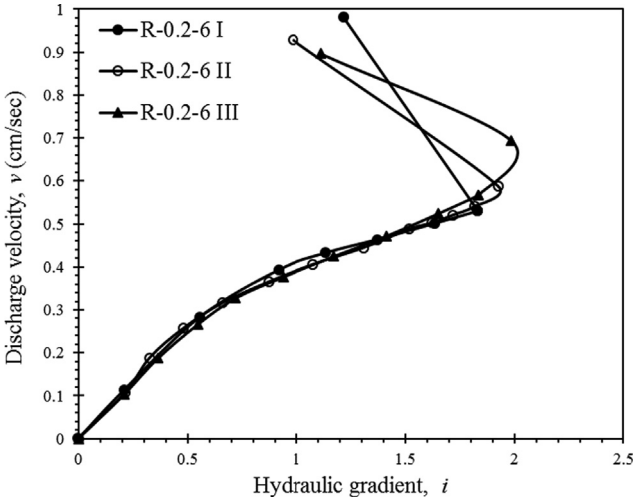

Fig. 5. Demonstration example of test replicability.

$$f(\theta) = \frac{\rho(\theta)\cos(\theta)}{\bar{\rho}} \tag{6}$$

The cumulative density function for fiber orientation within an angle of ±β from the horizontal is then calculated as:

$$F(\theta) = \frac{1}{2\bar{\rho}} \int_{-\beta}^{\beta} \rho(\theta)\cos(\theta)\mathrm{d}\theta \tag{7}$$

Eq. (7) could also be considered as the ratio of the volume of fibers with orientations within an angle of ±β from the horizontal to the total volume of fibers.

To obtain the fiber orientation parameters *A*, *B*, and *n* in Eqs. (4) and (5), three specimens (R-0.2-6, R-0.2-12, and R-0.2-19) were prepared following the procedure suggested by Diambra et al. [25]. When each specimen was prepared using the moist tamping technique, the fiber orientation distribution was largely independent of the fiber content [25,45]. Accordingly, only the influence of fiber length on fiber orientation was evaluated in fiber orientation analysis.

Fig. 6 shows photographs of the test specimens for fiber orientation analysis. The soil and fiber materials and the specimen preparation procedure were identical to those used in the seepage test. The soil was dyed black to create a color contrast with the fibers, which were white. The wet soil-fiber mixture was placed into a mold, after which the specimen within the mold was left in a freezer for 24 h. Then, the frozen specimen was removed from the mold and cut in half along either the vertical (Fig. 6a) or horizontal plane. The number of fibers in a selected 10 mm × 10 mm area was counted using a magnifying glass (Fig. 6b and c). The fiber-counting process was repeated at 20 different locations in the cut plane, and the average number of fibers for an area of 10 mm × 10 mm was obtained for the vertical and horizontal planes (denoted as N^V and N^H, respectively). The average N^V and N^H values of the three test specimens are listed in Table 5. The lower N^V value and higher N^H value (i.e., high N^V/N^H value) indicates the fibers are more visible in the horizontal cut plane than those in the vertical one, suggesting a higher probability of a large fiber orientation angle above the horizontal in this case.

After the N^V and N^H values were determined, the fiber orientation parameters *A*, *B*, and *n* were back-calculated using the following analytical equations for N^V and N^H from Eqs. (12) and (14) of Diambra et al. [25].

$$N^V = \frac{16 l_1 l_2}{V_{1f}} \int_0^{L_f/2} \left(\frac{1}{V_s} \int_0^{\cos^{-1}(b/R)} \int_0^{\alpha*} \rho(\theta) \frac{R^3}{3} \cos(\theta)\mathrm{d}\alpha\mathrm{d}\theta \right) \mathrm{d}b \tag{8}$$

$$N^H = \frac{4 l_1 l_2}{V_{1f}} \int_0^{L_f/2} \left(\frac{1}{V_s} \int_{\pi/2-\cos^{-1}(b/R)}^{\pi/2} \int_0^{2\pi} \rho(\theta) \frac{R^3}{3} \cos(\theta)\mathrm{d}\alpha\mathrm{d}\theta \right) \mathrm{d}b \tag{9}$$

where l_1 and l_2 are the length and width of the cut plane (=90 and 98 mm in this study); V_{1f} is the volume of a single fiber; *R* is the radius of the reference sphere that contains fibers with the midpoint coinciding with the center of the sphere (=L_f/2); V_s is the volume of the reference sphere (=$4\pi R^3/3 = \pi L_f^3/6$); *b* is the distance to the center of the reference sphere; αis the orientation angle on the horizontal plane; and the rest of the parameters have been defined earlier.

As shown in Table 5, the back-calculated fiber orientation parameter values yielded a reasonable match between the predicted values (i.e., N^V, N^H, and N^V/N^H) and the measured values. The model bias values (i.e., the ratio of the predicted N^V/N^H value to the measured value) were close to 1.0 for all three cases. By combining Eqs. (4) and (7) and entering the calibrated *A*, *B*, and *n* values, the cumulative density function for fiber orientation for the three specimens was obtained and presented in Fig. 7. Generally, 75% of fibers were oriented within ±30° of the horizontal plane for the specimens prepared using the moist tamping technique, implying that compacting the sand-fiber mixture during specimen preparation led to a preferential near-horizontal orientation for the fibers. Regarding the influence of fiber length on fiber orientation, under a given cumulative density value, the specimen with longer fibers has a larger orientation angle, suggesting the longer fibers are more likely to be bent, resulting in a larger orientation angle above the horizontal plane.

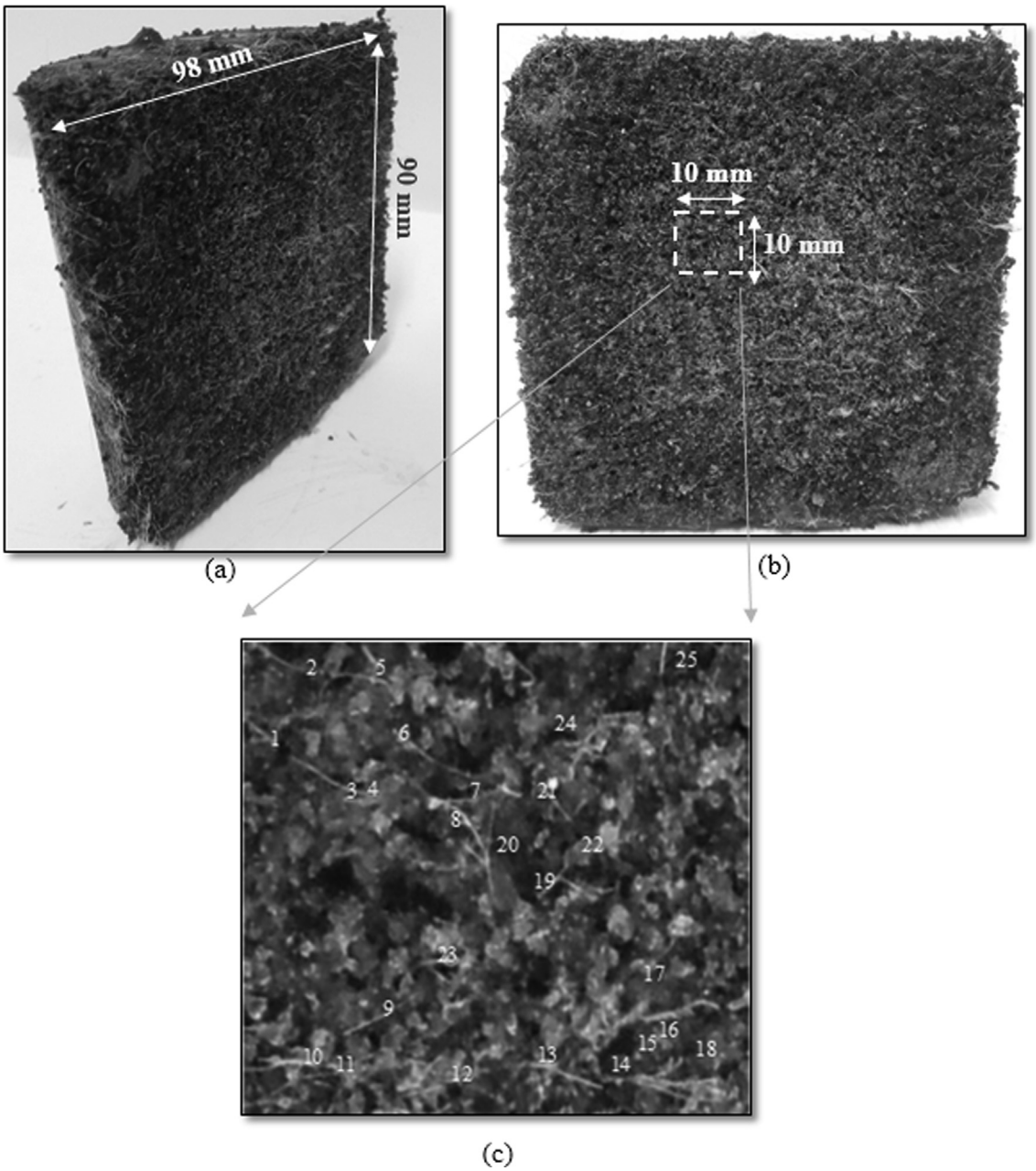

Fig. 6. Specimen for fiber orientation analysis: (a) specimen cut vertically; (b) vertical plane of the specimen and counting area, (c) enlarged vision (×5) of the counting area and fiber numbers.

Table 5
Fiber orientation test results.

Specimen	Height (mm)	Diameter (mm)	Fiber gravimetric content, ω_f (%)	Fiber volumetric content, ρ_f (%)	Measured[1]			Orientation parameters			Predicted			
					N^V	N^H	N^V/N^H	A	n	B	N^V	N^H	N^V/N^H	Model bias[2]
R-0.2-6	90	98	0.2	0.33	24.83	12.67	1.96	0	5	2.04	24.80	12.24	2.03	1.04
R-0.2-12	90	98	0.2	0.33	24.67	13.13	1.88	0	4	1.88	24.52	13.14	1.87	0.99
R-0.2-19	90	98	0.2	0.33	23.83	14.5	1.64	0	3	1.7	24.13	14.28	1.69	1.03

[1] Number of fibers in a 10 mm × 10 mm area averaged from 20 different locations.
[2] Ratio of the predicted N^V/N^H value to the measured one.

The micro-scale structure of the FRS and soil-fiber interaction was observed using the mean of SEM images (Fig. 8). For unreinforced gap-graded soil (Fig. 8a), the fine particles partially filled the pore spaces formed by the coarse particle matrix. Because some pore sizes were larger than the fine particles, the fine particles can be eroded by seepage through the pore channels, leading to suffusion failure.

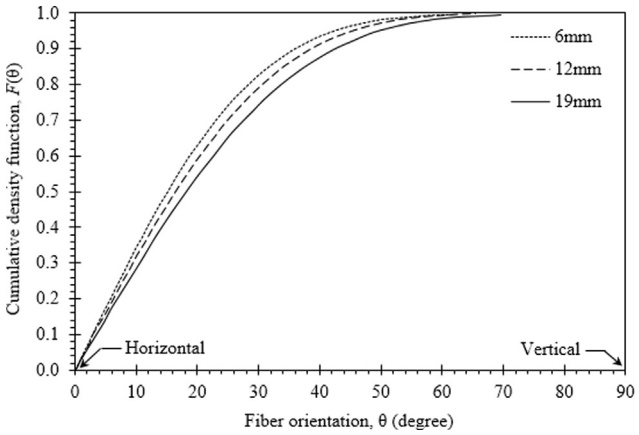

Fig. 7. Cumulative distribution function of fiber orientation distribution.

For the FRS (Fig. 8b and c), the pore spaces of soil were partially blocked, and the pore sizes were reduced by fibers. Two improvement functions provided by the fibers were observed. First, the randomly distributed fibers formed a net structure that held the fine particles in place and restricted fine-particle erosion with seepage flow (Fig. 8b). The dense netting effect prevails when the total number of fibers in FRS is high (i.e., high fiber content and short fiber length). Second, the fibers provided tensile resistance to enhance soil shear strength and prevent an increase in soil volume induced by seepage (Fig. 8c). This reinforcing effect is most efficacious when the fiber orientation is parallel to the seepage direction (i.e., the vertical direction in this case). A strong vertical reinforcing effect is expected to occur in the FRS with long fibers, which has a high probability of a fiber orientation angle above horizontal as demonstrated in the fiber orientation analysis. Fig. 9 illustrates these two improvement mechanisms in accordance with different fiber amounts and lengths.

4. Results and discussion

Seepage test results related to the soil erosion process, hydraulic gradient and seepage discharge velocity (i–v) relations, and failure modes are presented and discussed in this section. The i–v plots are used to determine the hydraulic conductivity, critical hydraulic gradient, and Forchheimer coefficients of FRS for further comparison.

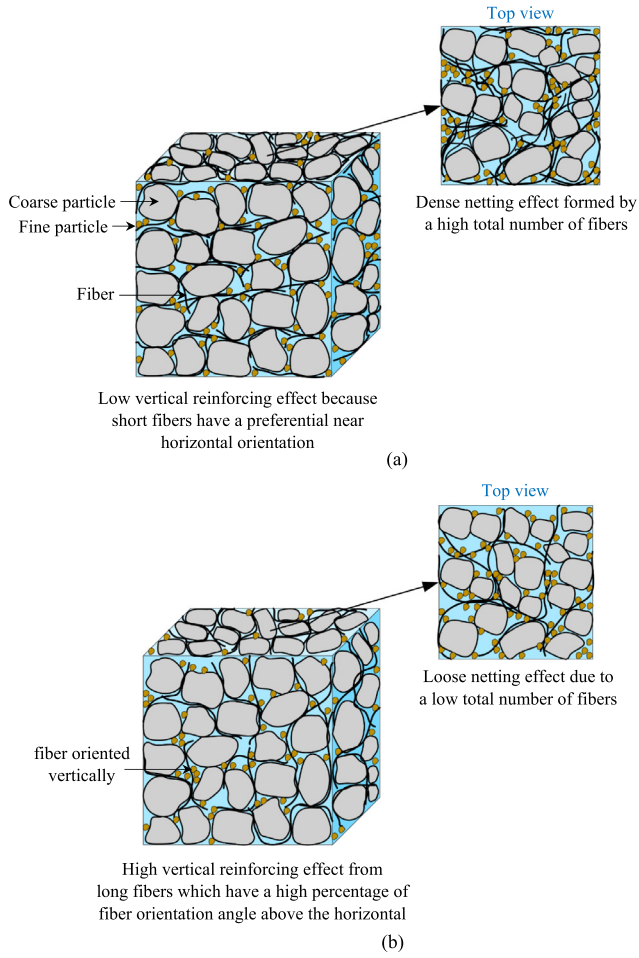

Fig. 9. Illustrations of soil-fiber interaction and improving mechanism: (a) FRS with short fibers and a high fiber content; (b) FRS with long fibers and a low fiber content.

4.1. Determination of critical hydraulic gradients

As reported in the literature, critical hydraulic gradients can be determined at various stages of the internal erosion process [13]. In this study, three identification methods, each representing different extents of fine fraction loss, were adopted to determine the

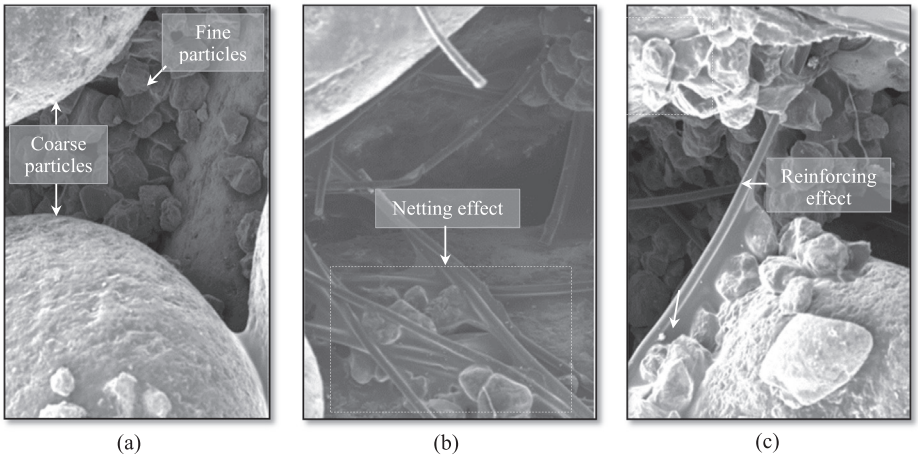

Fig. 8. Scanning electron microscope (SEM) photographs: (a) unreinforced soil; (b) and (c) reinforced soil showing the soil-fiber interaction.

critical hydraulic gradient. The first method determines the critical hydraulic gradient at the onset of the internal erosion of fine particles (denoted as $i_{cr,onset}$). This can be observed from the beginning of local fine-particle migration on the top of the specimen (Figs. 10b and 11b).

The second method determines the critical hydraulic gradients based on the variation of soil permeability or flow conditions (denoted as $i_{cr,intersect}$). A change in soil permeability implies an increase in soil porosity because fine particles are washed out from the pore spaces of the coarse fraction. This critical hydraulic gradient value can be determined numerically at the intersection of the two linear regression lines on the measured *i*-*v* curve (Figs. 10a–12a). The $i_{cr,intersect}$ determined using this method tends to be close to the turning point of the measured *i*-*v* curve. For all tests, the Reynolds number (Re) values calculated using the discharge velocity corresponding to $i_{cr,intersect}$ are generally close to 10 (Table 4), indicating a flow transition from laminar to turbulent conditions at Re = 10.

The third method determines the critical hydraulic gradient at soil hydraulic failure (denoted as $i_{cr,failure}$), revealed by the loss of a substantial number of fine particles or a significant change in soil volume. In addition, soil hydraulic failure is commonly associated with a decrease in the measured hydraulic gradient. A decline in the hydraulic gradient suggests a reduction in hydraulic head loss, where many fine particles that cause seepage energy loss were eroded from the soil skeleton during hydraulic failure.

Figs. 10–12 indicate examples of the critical hydraulic gradient determined using the three identification methods discussed previously. The critical hydraulic gradient values for all tests are summarized in Table 4, ranging from small to large in the order of $i_{cr,onset} < i_{cr,intersect} < i_{cr,failure}$. The test results show that the $i_{cr,onset}$ and $i_{cr,intersect}$ values are generally close compared with the $i_{cr,failure}$ value which represents the most severe case of fine-particle loss. The close values of $i_{cr,onset}$ and $i_{cr,intersect}$ reveal that only a small amount of fine fraction loss alters soil permeability and flow conditions.

4.2. Erosion process and failure modes

Fig. 10 displays the *i*-*v* curve of unreinforced gap-graded soil (Test G) and photographs at various stages of the erosion process, detailed as follows. From Stages 0–2 (i = 0–0.15), the measured v increased linearly with an increasing i. The flow was laminar according to Darcy's law and no noteworthy changes were detected in the specimen. At Stage 3 (i = 0.18), local fine-particle migration began, with local erosion appearing at the top of the specimen (Fig. 10b). After Stage 3, the measured v increased rapidly, and soil permeability changed from fine fraction control to coarse fraction control. In Stages 5–6 (i = 0.21–0.23), fine particles were continually and gradually eroded and remained on the top of the specimen. The piping of fine particles became general, and the washed-out fine particles covered the top surface of the specimen (Fig. 10c). At Stage 13 (i = 0.27), several fine particles were eroded, and vigorous fine-particle piping was observed on the top surface of the specimen (Fig. 10d). At the next hydraulic head increment (i.e., Stage 14), the decreased in the measured i value indicated that soil hydraulic failure occurred. No volumetric expansion of the specimen was observed at this stage. The deposit of fine particles on the top surface of the specimen was approximately 9 mm after stopping the seepage flow.

For Test G, the critical hydraulic gradient values determined using the three identification methods were $i_{cr,onset}$ = 0.18, $i_{cr,intersect}$ = 0.19, and $i_{cr,failur}$ = 0.27, substantially lower than those obtained using Terzaghi's method for internally stable soil ($i_{cr} = -\gamma'/\gamma_w$, where γ' is the submerged unit weight of soil and γ_w is the unit weight of water). The test results supported the findings of Skempton and Brogan [90] that the i_{cr} for internally unstable soil is between approximately one-fifth and one-third of the theoretical value suggested by Terzaghi [94]. Soil hydraulic failure modes were determined based on Fannin and Slangen [31]'s definition: general piping failure was considered as a seepage-induced volumetric expansion with little fine fraction loss, whereas suffusion failure was characterized as a considerable amount of fine fraction loss without any notable change in soil volume. According to Fannin and Slangen's definition, the failure mode of Test G was identified as suffusion failure.

Fig. 11 shows the test result of FRS for ω_f = 0.3% and L_f = 19 mm (Test R-0.3-19). The migration of local fine particles began at Stage 2 (i = 0.33; Fig. 11b). At Stage 14 (i = 0.71), eroded fine particles completely covered the top surface of the specimen. At Stage 16 (i = 2.28), the specimen displayed moderate piping of fines at the top (Fig. 11c). Then, at Stage 17, soil hydraulic failure occurred as the measured i decreased. No visible soil volumetric change was observed at the point of soil hydraulic failure. The deposit of fines on the top surface measured approximately 4 mm after the test (Fig. 11d). The determined critical hydraulic gradient values were $i_{cr,onset}$ = 0.33, $i_{cr,intersect}$ = 0.48, and $i_{cr,failur}$ = 2.28. The failure mode in this test was identified as suffusion failure. The erosion process and failure mechanism were generally similar to those in Test G, but the three determined critical hydraulic gradient values were higher, and the deposit of fines was thinner.

Fig. 12 shows the test results of FRS for ω_f = 0.3% and L_f = 6 mm (Test R-0.3–6). At Stage 4 (i = 0.71), local fine particles began to migrate. The particles exhibited small, jittery movements at the side of the specimen. At Stage 12 (i = 2.36), piping of fines was observed at several locations on the top of the specimen. The top area was partially covered by fine particles (Fig. 12b and c). When the next hydraulic head increment was applied (i.e., Stage 13), the specimen showed a sudden and notable heave (21 mm), followed by global piping and boiling of the entire specimen (Fig. 12d). Horizontal cracks were observed at this stage, indicating significant specimen distress due to upward seepage force. The observed horizontal cracks also revealed that the upward seepage-induced tensile force may have exceeded the tensile resistance provided by fibers in local areas within the specimen; consequently, soil particles in these areas tended to separate and consequently cracks developed. A significant decrease in the i and increase in the v were measured after soil piping failure. Although the system total head was increased by elevating the upper water reservoir, the drop in the hydraulic gradient after i_{cr} suggests the relief of accumulated porewater pressure within specimens at soil piping failure due to the development of horizontal cracks and volumetric expansion. A decline in the hydraulic gradient also indicates a reduction in hydraulic head loss because of the loosened soil packing state after the soil seepage failure. A hydraulic gradient drop has also been observed in experimental and field tests [74,77]. The determined critical hydraulic gradient values were $i_{cr,onset}$ = 0.71, $i_{cr,intersect}$ = 0.73, and $i_{cr,failur}$ = 2.36. Based on the global soil piping and large volume change observed during seepage failure, the failure mode of this test was identified as a general piping failure.

Fig. 13 illustrates the observed failure modes associated with different fiber-reinforcing mechanisms. Table 6 lists the observed failure modes and associated failure conditions in terms of the fine deposit thickness and specimen volumetric heave. For Test G, the unreinforced gap-graded soil exhibited typical suffusion failure because considerable fine particles were washed out of the soil structure during testing (Fig. 13a). For Test R-0.3-19, the FRS mixed with long fibers or low fiber content, with a low total number of fibers, formed a relatively loose netting effect to reduce pore size and restrict fine-particle erosion (Fig. 13b). Consequently, suffusion failure was still observed at seepage failure, but fewer fine particles were washed out compared with the unreinforced case. For Test R-0.3-6, the FRS mixed with short fibers and high fiber

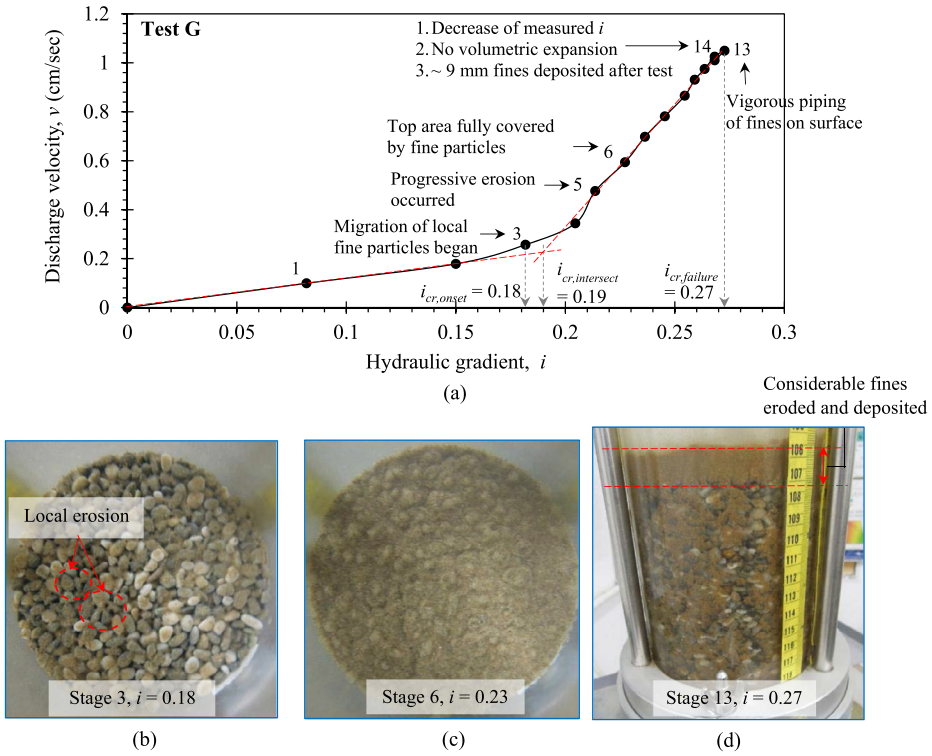

Fig. 10. Test results of unreinforced gap-graded soil: (a) *i*-*v* curve, (b) onset of erosion, (c) top area was fully covered by fine particles, (d) at hydraulic failure.

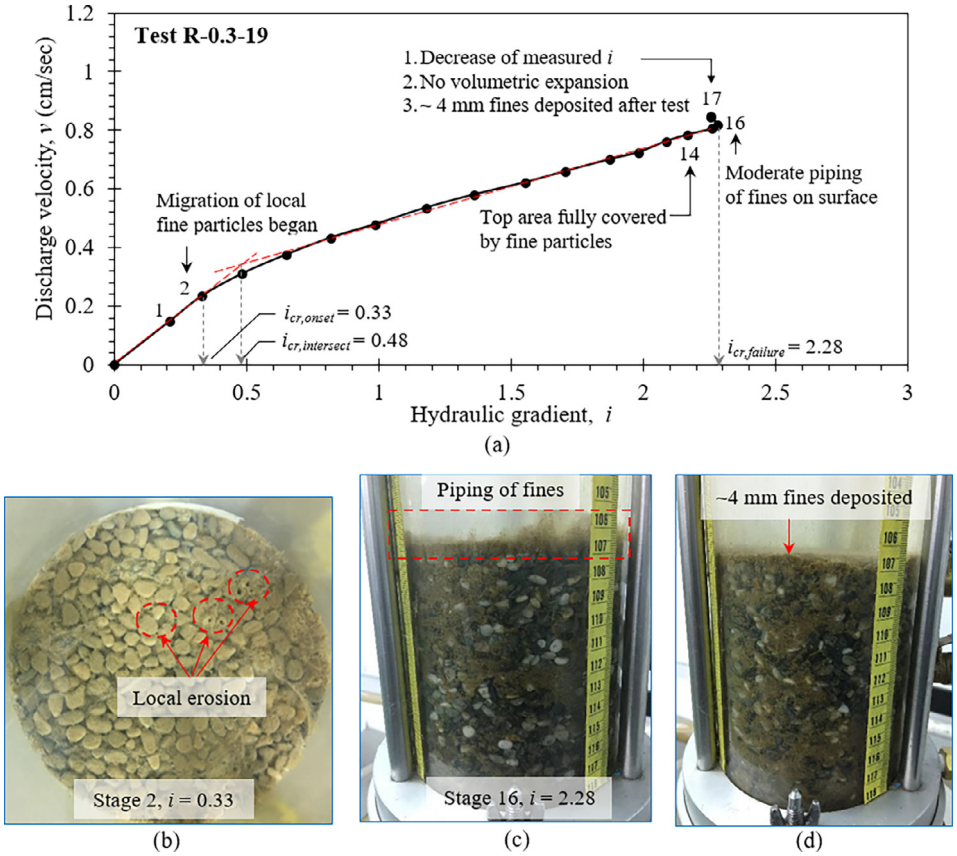

Fig. 11. Test results of R-0.3-19: (a) *i*-*v* curve, (b) onset of erosion, (c) at hydraulic failure, (d) after test.

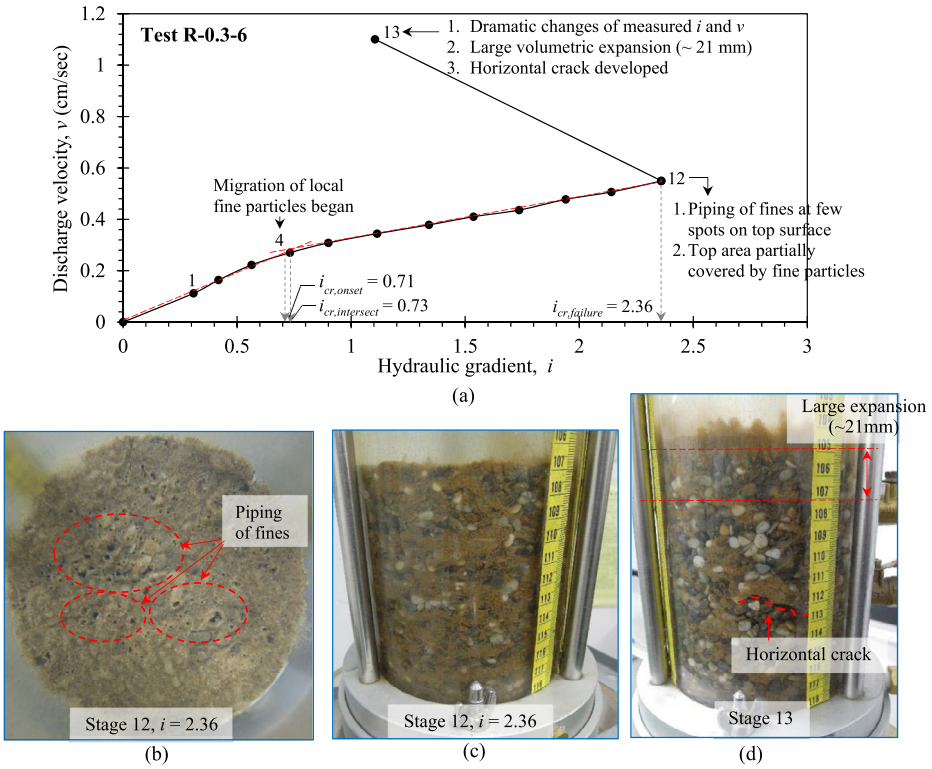

Fig. 12. Test results of R-0.3-6: (a) *i-v* curve, (b) and (c) at hydraulic failure, (d) at the next applied hydraulic head increment after $i_{cr,\ failure}$.

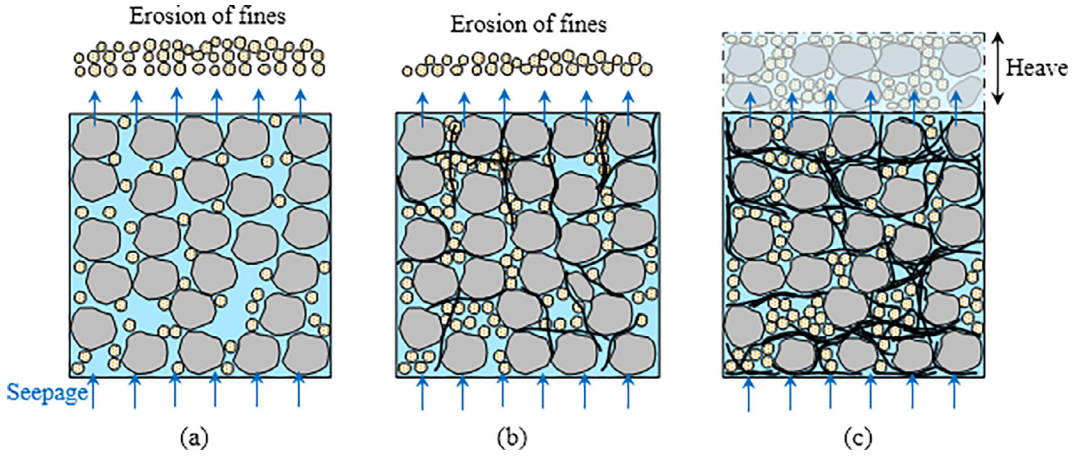

Fig. 13. Illustrations of failure modes: (a) unreinforced soil-suffusion; (b) FRS with long fiber or low fiber content-suffusion; (c) FRS with short fiber or high fiber content-piping.

Table 6
Failure mode and the associated failure conditions.

Test	Failure mode	Thickness of fine deposit (mm)	Specimen heave (mm)
C	No Failure	–	–
F	Piping	–	60
G	Suffusion	9	–
R-0.1-6	Suffusion	4	–
R-0.2-6	Piping	–	15
R-0.3-6	Piping	–	21
R-0.1-12	Suffusion	8	–
R-0.2-12	Suffusion	4	–
R-0.3-12	Piping	–	20
R-0.1-19	Suffusion	9	–
R-0.2-19	Suffusion	5	–
R-0.3-19	Suffusion	4	–

content, with a high total number of fibers, contributed to a relatively dense netting effect (Fig. 13c). When the fiber-reduced pore size was smaller than the size of fine particles, fine particles were mostly retained by the fibers and the mobility of fine particles with seepage was limited, resulting in the soil failed hydraulically in the general-piping-type failure mode rather than through suffusion. The dense fiber netting effect can effectively bind soil particles together; thus, a large seepage force is required to cause soil failure. Once the seepage force exceeds the soil resistance, soil hydraulic failure occurs and most pore spaces are forced to open simultaneously, causing an observable volume expansion in the specimen, a sudden release of hydraulic pressure, and a substantial increase in seepage velocity.

4.3. Overall test results

The overall test results are discussed and compared in this section. Fig. 14 displays the measured *i*-*v* curves for all tests, and Table 4 summarizes the corresponding hydraulic parameters determined from the measured *i*-*v* curves. The test results of unreinforced uniform coarse and fine sand (Tests C and F, respectively) are also plotted in Fig. 14 to provide a reference for the upper and lower test limits. For Test C (unreinforced coarse sand), no seepage failure (neither erosion nor volumetric expansion) was observed at the end of the test when the system reached maximum capacity. The conditions of coarse sand under initial condition and at the end of the test are almost identical. The critical hydraulic gradient cannot be reached because the large pore spaces of the coarse sand caused little seepage head loss (or slight increment of the hydraulic gradient) in coarse sand. For Test F (unreinforced fine sand), the soil general piping occurred and sand boiling was observed after failure. The measured critical hydraulic gradient (i_{cr} = 1.01) upon soil hydraulic failure agrees well with the value predicted by Terzaghi's theoretical value for internally stable soil based on effective stress equal to zero.

The *i*-*v* curves of FRS in Fig. 14 consist of two parts: the first part is a linear, laminar Darcy flow in which hydraulic conductivity can be obtained according to Darcy's law (i.e., $v = ki$); the second part is a flow transition from laminar to turbulent conditions beyond the turning point of the *i*-*v* curve, also known as a non-Darcian flow. The decrease in the slope of the second part of the *i*-*v* curve was due to energy loss induced by the inertial effect of the eddies, which form a closed streamline and consume substantial energy when the seepage flows through the pore channels [88]. The Forchheimer equation [35,88] was used to determine the hydraulic parameters in the non-Darcian flow regime.

$$i = \frac{\mu}{\kappa \rho g} v + \frac{\beta}{g} v^2 \tag{10}$$

where κ and β are Forchheimer coefficients; μ is the dynamic viscosity of the fluid; ρ is the flow density; g is the gravitational acceleration; v is the flow velocity. The Forchheimer coefficient κ represents intrinsic permeability, which is independent of the flow properties and temperature effect and is correlated to hydraulic conductivity k as follows:

$$\kappa = \frac{k\mu}{\rho g} \tag{11}$$

The Forchheimer coefficient β reflects seepage energy loss, depending only on the properties (i.e., geometry and roughness) of the porous medium. The determined k, κ, and β values are listed in Table 4 and are discussed in the following paragraphs.

Fig. 14 shows that the *i*-*v* curves of all FRS appear at the right side of those for Test G, indicating that fiber reinforcement effectively enhances the internal erosion resistance of the soil by deferring the occurrence of soil piping at a high hydraulic gradient. Fig. 14 also indicates that the observed failure mode for Tests R-0.3-12, R-0.3-6, and R-0.2-6 was general piping, whereas that of all other tests was suffusion. A stability boundary based on the different failure modes is plotted in Fig. 14. Suffusion failure of FRS is observed if its *i*-*v* curve appears above this boundary, whereas general piping failure is identified if the *i*-*v* curve is below this boundary.

Table 4 lists the values of the normalized number of fibers (N_f), defined as the ratio of the number of fibers in a soil specimen to the number of 6-mm fibers required to fill the full void in the specimen. The N_f value can be obtained numerically using the weight–volume relationships of soil and fibers. When FRS has a high total number of fibers (i.e., N_f > 1%), the failure mode changes from suffusion to general piping because the dense netting effect generated by the high total number of fibers effectively reduces soil pore size, retains the fine fraction in place, restricts fine-particle migration, and binds soil particles together. This process leads to a transformation of soil from an internally unstable state to an internally stable state.

4.4. Influence of fiber parameters

Fig. 15 displays the influence of fiber parameters on the Forchheimer coefficients κ and β, showing a clear trend of decreasing κ

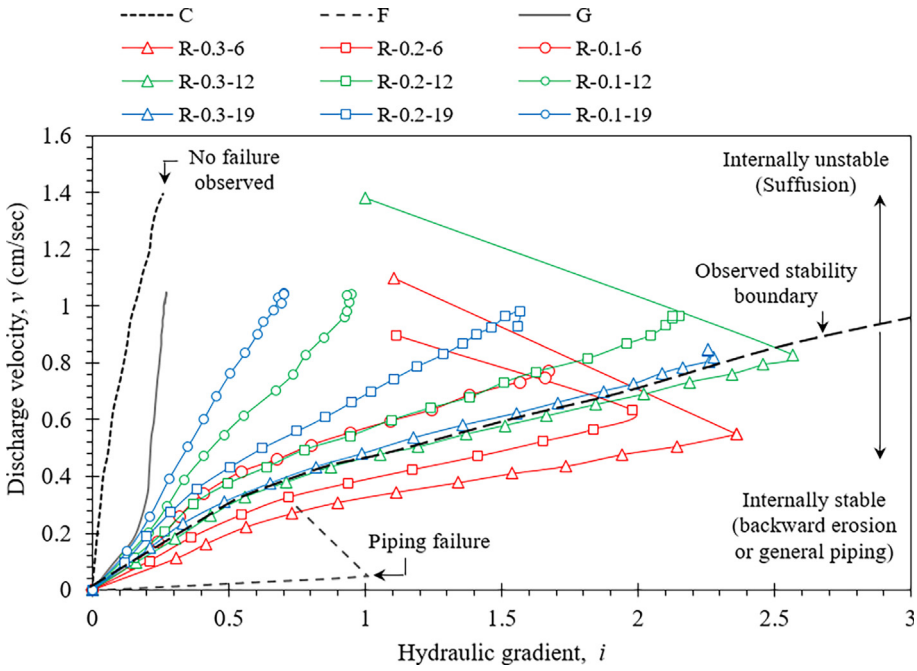

Fig. 14. *i*-*v* curves of all tests.

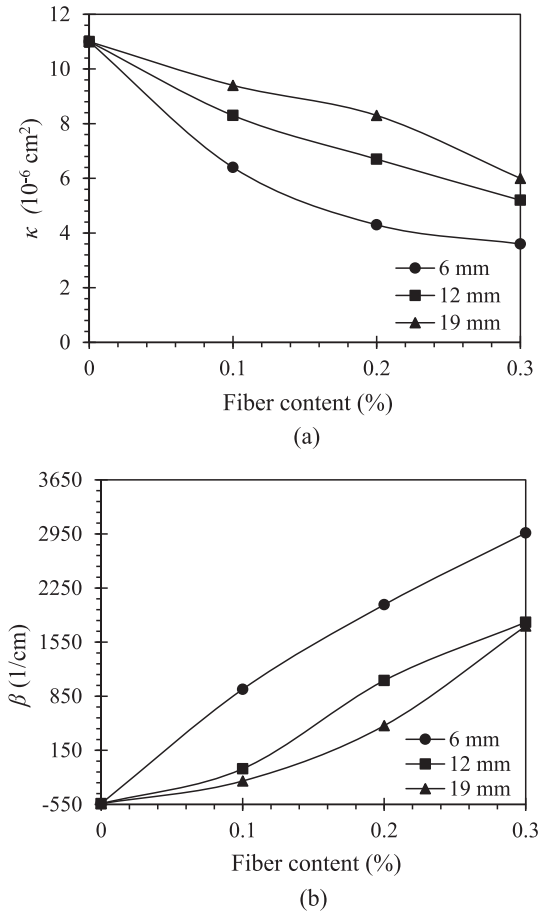

Fig. 15. Effect of fiber parameters on Forchheimer coefficients: (a) κ; (b) β.

and increasing β with increasing fiber content. As fiber content increases, more pore spaces can be blocked or filled by fibers, resulting in a greater reduction in soil permeability and increased seepage energy loss when seepage flow passes through the soil. Compared with FRS with long fibers at a given fiber content, FRS with short fibers can produce a larger decrease in κ and increase in β because of the dense netting effect resulting from the high number of fibers in the soil. In addition, FRS with long fibers has a fiber orientation less perpendicular to the seepage flow direction, which makes fibers less effective in restricting seepage flow passage.

Fig. 16 shows the influence of fiber parameters on i_{cr} at various stages of the erosion process. A clear increasing trend in i_{cr} with increasing fiber content can be observed for all i_{cr} values at three stages of the erosion process: two- to three-fold increases in $i_{cr,onset}$ and $i_{cr,intersect}$ as well as a more than five-fold increase in $i_{cr,\ failure}$ when the fiber content increases from 0% to 0.3%. The test results demonstrated that the internal erosion resistance of soil against suffusion can be effectively improved by adding a small amount of fiber into the soil. Short fibers have a more pronounced effect on improving internal erosion resistance than do long fibers; as noted, short fibers have a high number of fibers and can produce a dense netting effect.

The relationships between the three i_{cr} values and the normalized number of fibers N_f are further examined and depicted in Fig. 17. Unique linear relationships can be found for $i_{cr,onset}$ and $i_{cr,intersect}$ with N_f (Fig. 17a and b). The $i_{cr,onset}$ and $i_{cr,intersect}$ increase as N_f increases, suggesting that the total number of fibers is the primary factor affecting soil erosion resistance at the initial stage of the erosion process. The dense netting effect produced by a high number of fibers is likely to either keep the fine particles in place or capture the eroded particles, thereby delaying fine-particle migration.

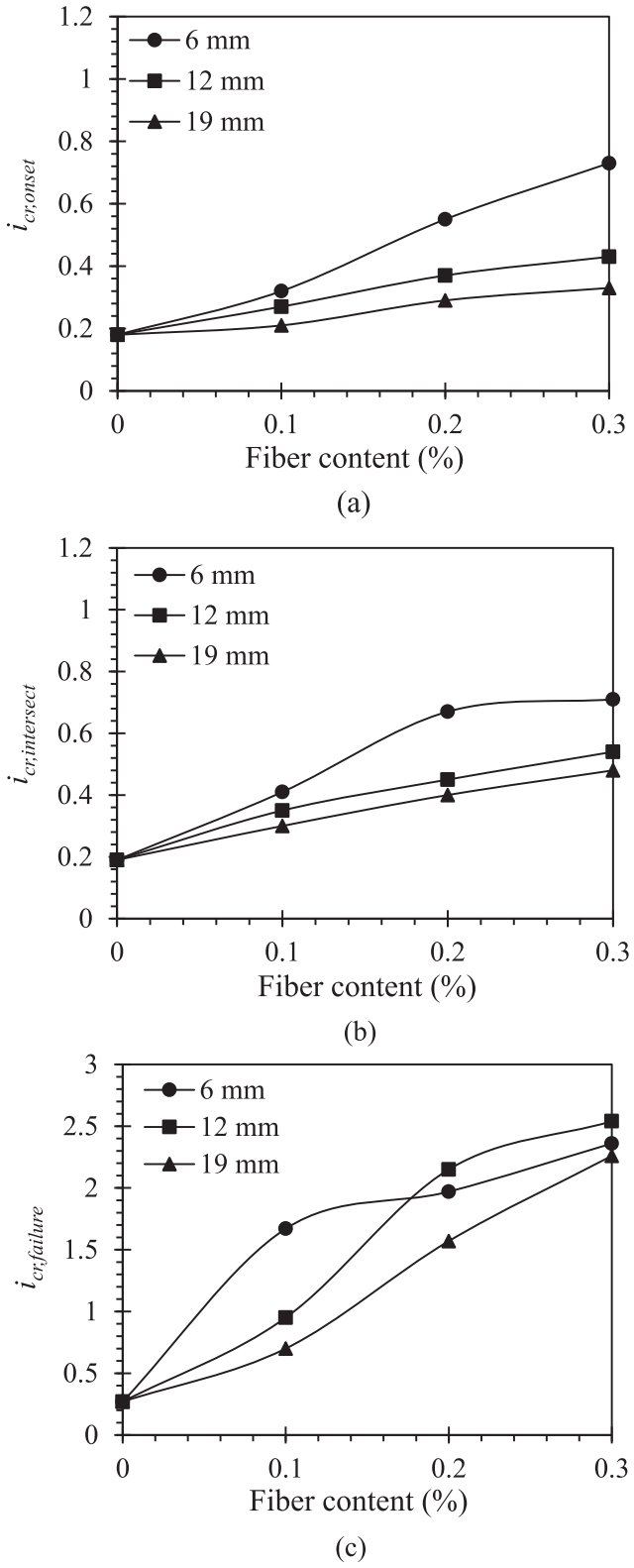

Fig. 16. Effect of fiber parameters on various critical hydraulic gradients: (a) $i_{cr,onset}$; (b) $i_{cr,intersect}$; (c) $i_{cr,failure}$.

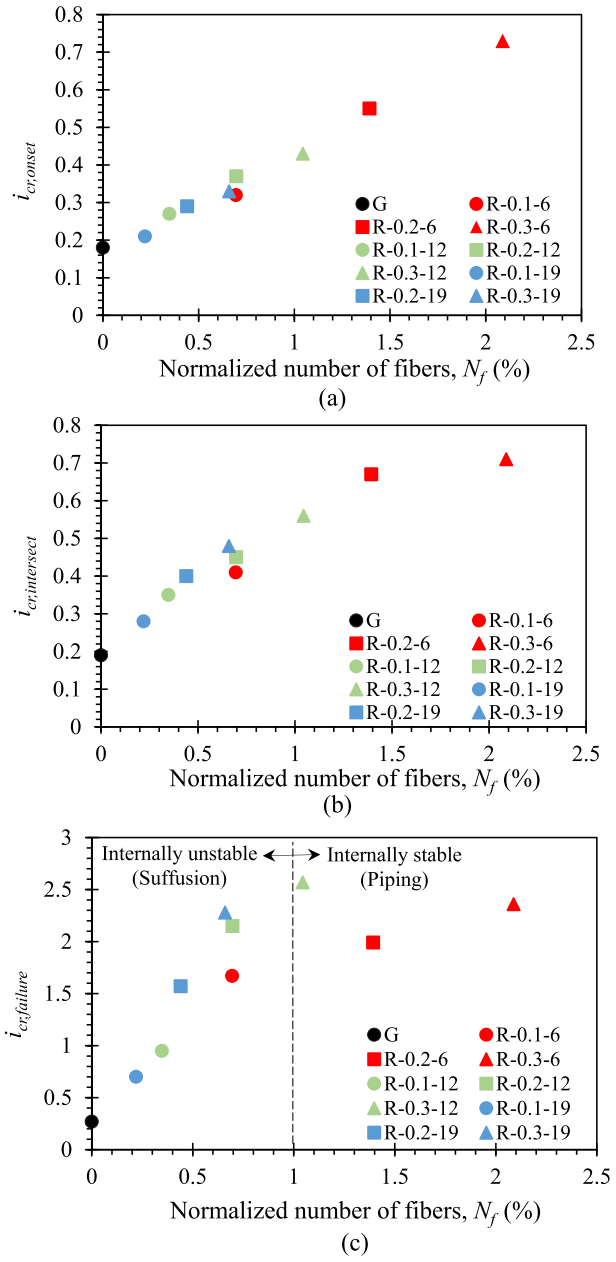

Fig. 17. Relationships between number of fibers various critical hydraulic gradients: (a) $i_{cr,onset}$; (b) $i_{cr,intersect}$; (c) $i_{cr,failure}$.

In terms of the relationship between $i_{cr,\ failure}$ and N_f (Fig. 17c), a linear relationship still applies for FRS, which fails in suffusion when $N_f < 1\%$. The increasing trend of $i_{cr,failure}$ with N_f suggests that $i_{cr,\ failure}$ is mainly governed by the fiber netting effect in the suffusion failure mode. However, the linear relationship is not applicable to FRS in the piping failure mode when $N_f > 1\%$. The $i_{cr,\ failure}$ seems not to be a function of the total number of fibers. Test R-0.3–12 with a lower N_f value ($N_f = 1.04$) has a higher $i_{cr,\ failure}$ value than Test R-0.3–6 ($N_f = 2.08$) and Test R-0.2–6 ($N_f = 1.39$). In this case, the fiber length affects the $i_{cr,failure}$ value: FRS with long fibers demonstrates a high critical hydraulic gradient at soil hydraulic failure, presumably because the long fibers possess a strong vertical reinforcing effect (i.e., the second improvement mechanism as shown in Fig. 8c and discussed in Section 3). This attribute provides high tensile resistance to enhance soil resistance against general piping failure.

5. Conclusions

In this study, experimental seepage tests were conducted to investigate the hydraulic response, erosion process, failure mode, and critical hydraulic gradient of unreinforced soil and FRS. Fiber orientation and SEM analyses were performed to enhance understanding of the soil-fiber interaction and improvement mechanisms. The effectiveness of adding fiber and the influence of fiber parameters (i.e., fiber content, length, and total number of fibers) on improving the internal erosion resistance of soil against suffusion was evaluated quantitatively. Based on the experimental results and analyses, key findings are summarized as follows:

1. The test results indicated that the unreinforced gap-graded soil failed in a suffusion failure mode with a considerable number of fine particles having been washed out. The measured i_{cr} value was substantially lower than Terzaghi's theoretical value.
2. This study revealed that the internal erosion resistance of soil against suffusion can be effectively improved by adding a small number of fibers into the soil. Fiber improves erosion resistance in two mechanisms: the fiber netting effect, which can hold fine particles in place and restrict migration of eroded fine particles; and the vertical reinforcing effect, in which fibers provide tensile resistance to enhance soil shear strength and prevent a seepage-induced soil volume increase.
3. The netting effect prevails when the total number of fibers in FRS is high (i.e., high fiber content and short fiber length), whereas the vertical reinforcing effect is most efficacious for FRS with long fibers.
4. The hydraulic failure mode of FRS is influenced by the total number of fibers. For FRS with a low total number of fibers (i.e., $N_f < 1\%$), the failure mode was identified as suffusion failure. The erosion process and failure mechanism were similar to those of unreinforced gap-graded soil (Test G), but the i_{cr} values determined at various stages were higher, and the deposit of fines was thinner.
5. For FRS with a high total number of fibers (i.e., $N_f > 1\%$), the dense netting effect results in only slight erosion of fine particles during testing. The general piping failure mode occurs with a sudden and notable volumetric heave at the point of seepage failure.
6. The failure mode of gap-graded soil could change from suffusion into general piping by adding sufficient fibers, implying that gap-graded soil is transformed from internally unstable soil into internally stable soil.
7. A clear increasing trend in i_{cr} with increasing fiber content was observed for all three stages of the erosion process (determined at the onset of internal erosion, at the flow transition from laminar to turbulent conditions, and at soil hydraulic failure). The $i_{cr,onset}$ and $i_{cr,intersect}$ increased two- to three-fold, and $i_{cr,\ failure}$ increased more than five times when the fiber content increased from 0 to 0.3%.
8. Unique linear relationships were identified for $i_{cr,onset}$ and $i_{cr,intersect}$ with N_f : the $i_{cr,onset}$ and $i_{cr,intersect}$ increased as N_f increased, suggesting that the total number of fibers is a primary factor affecting soil erosion resistance at the early phase of the erosion process.
9. A linear relationship between $i_{cr,\ failure}$ and N_f still applies for FRS in suffusion failure mode ($N_f < 1\%$). However, the $i_{cr,\ failure}$ does not appear to be a function of N_f for FRS in the piping failure mode ($N_f > 1\%$). In this case, the fiber length affects the $i_{cr,failure}$ value: FRS with long fibers produces a high $i_{cr,failure}$ value because long fibers have a strong vertical reinforcing effect that provides high tensile resistance to enhance soil resistance against general piping failure.

This study tested only one fiber type (i.e., PP fiber) with the same fiber diameter. The effects of fiber type and diameter on the internal erosion resistance of FRS are noteworthy topics for further evaluation. Furthermore, deterministic and probabilistic analyses are suggested to be performed to quantify the reduction in pore size when adding a certain number of fibers. The modified internal stability criteria considering the influence of fibers can then be established to identify the internal stability of FRS.

Declaration of Competing Interest

The authors declare that they have no potential conflict of interest with other researchers and organizations.

Acknowledgments

The financial support for this research was from the Ministry of Science and Technology of Taiwan under grant no. MOST105-2221-E-011-038. The financial support for the third author was provided by the Taiwan Ministry of Education under the grant for "Aim for the Top-Tier University Project". These financial supports are gratefully acknowledged.

References

[1] B.T. Adams, M. Xiao, A. Wright, Erosion mechanisms of organic soil and bioabatement of piping erosion of sand, J. Geotech. Geoenviron. Eng., ASCE 139 (8) (2013) 1360–1368.
[2] M.F. Ahlinhan, M. Achmus, Experimental investigation of critical hydraulic gradients for unstable soils, Scour Erosion, ASCE (2010) 599–608.
[3] F. Ahmad, F. Bateni, M. Azmi, Performance evaluation of silty sand reinforced with fibres, Geotext. Geomembr. 28 (1) (2010) 93–99.
[4] O. Akay, A.T. Özer, G.A. Fox, G.V. Wilson, Application of fibrous streambank protection against groundwater seepage, J. Hydrol. 565 (2018) 27–38.
[5] O. Akay, A.T. Özer, G.A. Fox, G.V. Wilson, Fiber reinforced sandy slopes under groundwater return flow, J. Irrig. Drain., ASCE 144 (5) (2018) 04018004.
[6] O. Akay, A.T. Ozer, G.A. Fox, G.V. Wilson, Behavior of fiber-reinforced sandy slopes under seepage, World Environ. Water Resour. Congr. (2016) 397–406.
[7] ASTM D2434, Standard Test Method for Permeability of Granular Soils (Constant Head). ASTM International, West Conshohocken, PA, USA.
[8] ASTM D4253, Standard Test Methods for Maximum Index Density and Unit Weight of Soils using a Vibratory Table. ASTM International, West Conshohocken, PA, USA.
[9] ASTM D4254, Standard Test Methods for Minimum Index Density and Unit Weight of Soils and Calculation of Relative Density. ASTM International, West Conshohocken, PA, USA.
[10] F. Bendahmane, D. Marot, A. Alexis, Experimental parametric study of suffusion and backward erosion, *J. Geotech. Geoenviron. Eng.*, ASCE 134 (1) (2008) 57–67.
[11] D.S. Chang, L.M. Zhang, Internal stability criteria for soils, Rock Soil Mech. 32 (2011) 253–259 (in Chinese).
[12] D.S. Chang, L.M. Zhang, Critical hydraulic gradients of internal erosion under complex stress states, J. Geotech. Geoenviron. Eng. 139 (9) (2013) 1454–1467.
[13] D.S. Chang, L.M. Zhang, Extended internal stability criteria for soils under seepage, Soils Found. 53 (4) (2013) 569–583.
[14] H. Choo, B. Yoon, W. Lee, C. Lee, Evaluation of compressibility and small strain stiffness characteristics of sand reinforced with discrete synthetic fibers, Geotext. Geomembr. 45 (4) (2017) 331–338.
[15] R. Collins, M. Zhang, X. Zhang, L. Hulsey, T. Ravens, R. Van Veldhuizen, Evaluation of geofibers and nontraditional liquid additives on erodible slopes in Interior Alaska, Geotext. Geomembr. 43 (5) (2015) 412–423.
[16] N.C. Consoli, M. Casagrande, M. Coop, Performance of a fibre-reinforced sand at large shear strains, Géotechnique 57 (9) (2007) 751–756.
[17] N.C. Consoli, R.R. de Moraes, L. Festugato, Split tensile strength of monofilament polypropylene fiber-reinforced cemented sandy soils, Geosynth. Int. 18 (2) (2011) 57–62.
[18] N.C. Consoli, P. Montardo, M. Prietto, S. Pasa, Engineering behavior of a sand reinforced with plastic waste, *J. Geotech. Geoenviron. Eng.* ASCE 128 (6) (2002) 462–472.
[19] J. Danka, L.M. Zhang, Dike failure mechanisms and breaching parameters, *J. Geotech. Geoenviron. Eng.*, ASCE 141 (9) (2015) 04015039.
[20] A. Das, Ch. Jayashree, B.V.S. Viswanadham, Effect of randomly distributed geofibers on the piping behaviour of embankments constructed with fly ash as a fill material, Geotext. Geomembr. 27 (5) (2009) 341–349.
[21] A. Das, B.V.S. Viswanadham, Experiments on the piping behavior of geofiber-reinforced soil, Geosynth. Int. 17 (4) (2010) 171–182.
[22] M. De Camillis, G. Di Emidio, A. Bezuijen, R.D. Verástegui-Flores, Hydraulic conductivity and swelling ability of a polymer modified bentonite subjected to wet–dry cycles in seawater, Geotext. Geomembr. 44 (5) (2016) 739–747.
[23] A. Diambra, E. Ibraim, Fibre-reinforced sand: interaction at the fibre and grain scale, Géotechnique 65 (4) (2015) 296–308.
[24] A. Diambra, E. Ibrahim, D. Mui Wood, A.R. Russell, Fiber reinforced sands: experiments and modelling, Geotext. Geomembr. 28 (3) (2010) 238–250.
[25] A. Diambra, A.R. Russell, E. Ibraim, D.M. Wood, Determination of fibre orientation distribution in reinforced sands, Geotechnique 57 (7) (2007) 623–628.
[26] P.V. Divya, B.V.S. Viswanadham, J.P. Gourc, Hydraulic conductivity behavior of soil blended with geofiber inclusions, Geotext. Geomembr. 46 (2018) 121–130.
[27] M.B. Esfandiari Sowmehsaraei, R. Jamshidi Chenari, Investigation on the effect of carpet fiber inclusion on hydraulic conductivity of clean sand using laboratory and random finite element analyses, Int. J. Civ. Eng. 12 (1 and B) (2014) 72–79.
[28] A.R. Estabragh, A. Soltanijad, A.A. Javadi, Models for predicting the seepage velocity and seepage force in a fiber reinforced silty soil, Comput. Geotech. 75 (2016) 174–181.
[29] A.R. Estabragh, K. Soltannajad, A.A. Javadi, Improving piping resistance using randomly distributed fibers, Geotext. Geomembr. 42 (1) (2014) 15–24.
[30] R.J. Fannin, Karl Terzaghi: from theory to practice in geotechnical filter design, *J. Geotech. Geoenviron. Eng.*, ASCE 134 (2008) 267–276.
[31] R.J. Fannin, P. Slangen, On the distinct phenomena of suffusion and suffosion, Géotech. Lett. 4 (4) (2014) 289–294.
[32] R. Fell, J.-J. Fry, State of the art on the likelihood of internal erosion of dams and levees by means of testing, in: S. Bonelli (Ed.), Erosion in Geomechanics Applied to Dams and Levees, Chapter 1, ISTE-Wiley, London, UK, 2013, pp. 1–99.
[33] R. Fell, C.F. Wan, J. Cyganiewicz, M. Foster, Time for development of internal erosion and piping in embankment dams, *J. Geotech. Geoenviron. Eng.*, ASCE 129 (4) (2003) 307–314.
[34] L. Festugato, E. Menger, F. Benezra, E.A. Kipper, N.C. Consoli, Fibre-reinforced cemented soils compressive and tensile strength assessment as a function of filament length, Geotext. Geomembr. 45 (1) (2017) 77–82.
[35] P. Forchheimer, Wasserbewegung durch Boden, Z. Ver. Dtsch., Ingenieuer. 45 (1901) 1782–1788.
[36] M. Foster, R. Fell, M. Spannagle, The statistics of embankment dam failures and accidents, Can. Geotech. J. 37 (5) (2000) 1000–1024.
[37] J.-J. Fry, Introduction to the process of internal erosion in hydraulic structures: embankment dams and dikes, in: S. Bonelli (Ed.), Erosion of Geomaterials, Chapter 1, ISTE-Wiley, London, UK, 2012, pp. 1–36.
[38] K. Furumoto, H. Miki, N. Tsuneoka, T. Obata, Model test on the piping resistance of short fiber reinforced soil and its application to river levee, in: Proceeding of the 7th International Conference on Geosynthetics, Nice, France, 2002, pp. 1241–1244.
[39] S.J. Garner, R.J. Fannin, Understanding internal erosion: a decade of research following a sinkhole event, Int. J. Hydropower Dams 17 (3) (2010) 93–98.
[40] D. Gray, T. Al-Refeai, Behavior of fabric-versus fiber-reinforced sand, *J. Geotech. Eng.*, ASCE 112 (8) (1986) 804–820.
[41] D.J. Hagerty, Piping/sapping erosion. I: basic considerations, *J. Hydraul. Eng.*, ASCE 117 (8) (1991) 991–1008.
[42] D.J. Hagerty, Piping/sapping erosion. II: identification-diagnosis, *J. Hydraul. Eng.* ASCE 117 (8) (1991) 1009–1025.
[43] S.M. Hejazi, M. Sheikhzadeh, S.M. Abtahi, A. Zadhoush, A simple review of soil reinforcement by using natural and synthetic fibers, Constr. Build. Mater. 30 (2012) 100–116.
[44] M.S. Hosney, R.K. Rowe, Performance of polymer-enhanced bentonite–sand mixture for covering arsenic-rich gold mine tailings for up to 4 years, Can. Geotech. J. 54 (4) (2017) 588–599.
[45] E. Ibraim, A. Diambra, A.R. Russell, D. Muir Wood, Assessment of laboratory sample preparation for fibre reinforced sands, Geotext. Geomembr. 34 (2012) 69–79.
[46] B. Indraratna, V.T. Nguyen, C. Rujikiatkamjorn, Assessing the potential of internal erosion and suffusion of granular soils, *J. Geotech. Geoenviron. Eng.*, ASCE 137 (5) (2011) 550–554.
[47] V.S. Istomina, Filtration Stability of Soils, Gostroizdat, Moscow, Leningrad, 1957 (in Russian).
[48] M. Jamei, P. Villard, H. Guiras, Shear failure criterion based on experimental and modeling results for fiber-reinforced clay, *Int. J. Geomech.* ASCE 13 (6) (2013) 882–893.
[49] P. Jamsawang, P. Voottipruex, S. Horpibulsuk, Flexural strength characteristics of compacted cement-polypropylene fiber sand, *J. Mater. Civ. Eng.* ASCE 27 (9) (2015) 04014243.
[50] R. Jamshidi, I. Towhata, H. Ghiassian, R. Tabarsa, Experimental evaluation of dynamic deformation characteristics of sheet pile retaining walls with fiber reinforced backfill, Soil Dyn. Earthquake Eng. 30 (6) (2010) 438–446.
[51] G.M. Kanchi, V.S. Neeraja, G.L.S. Babu, Effect of anisotropy of fibers on the stress-strain response of fiber-reinforced soil, *Int. J. Geomech.* ASCE 15 (1) (2015) 06014016.
[52] L. Ke, A. Takahashi, Strength reduction of cohesionless soil due to internal erosion induced by one-dimensional upward seepage flow, Soils Found. 52 (4) (2012) 698–711.
[53] L. Ke, A. Takahashi, Experiment investigations on suffusion characteristics and its mechanical consequences on saturated cohesionless soil, Soils Found. 54 (4) (2014) 713–730.

[54] T.C. Kenney, D. Lau, Internal stability of granular filters, Can. Geotech. J. 22 (2) (1985) 215–225.
[55] T.C. Kenney, D. Lau, Internal stability of granular filters: reply, Can. Geotech. J. 23 (3) (1986) 420–423.
[56] A.R.D. Kézdi, Soil Physics: Selection Topics (Developments in Geotechnical Engineering), Elsevier Science Ltd., Amsterdam, Netherlands, 1979.
[57] M.J. Khattak, M. Alrashidi, Durability and mechanistic characteristics of fiber reinforced soil–cement mixtures, Int. J. Pavement Eng. 7 (1) (2006) 53–62.
[58] C. Li, J. Zornberg, Mobilization of reinforcement forces in fiber-reinforced soil, *J. Geotech. Geoenviron. Eng.*, ASCE 139 (1) (2013) 107–115.
[59] H. Li, K. Senetakis, A. Khoshghalb, On the small-strain stiffness of polypropylene fibre-sand mixtures, Geosynth. Int. 26 (1) (2019) 66–80.
[60] H. Li, K. Senetakis, Dynamic properties of polypropylene fibre-reinforced silica quarry sand, Soil Dyn. Earthquake Eng. 100 (2017) 224–232.
[61] J. Li, C. Tang, D. Wang, X. Pei, B. Shi, Effect of discrete fibre reinforcement on soil tensile strength, J. Rock Mech. Geotech. Eng. 6 (2) (2014) 133–137.
[62] M. Li, R.J. Fannin, Comparison of two criteria for internal stability of granular soil, Can. Geotech. J. 45 (9) (2008) 1303–1309.
[63] M. Li, R.J. Fannin, A theoretical envelope for internal stability of cohesionless soil, Geotechnique 62 (1) (2012) 77–80.
[64] M. Li, R.J. Fannin, Capillary tube model for internal stability of cohesionless soil, *J. Geotech. Geoenviron. Eng.*, ASCE 139 (5) (2013) 831–834.
[65] J. Liu, G. Wang, T. Kamai, F. Zhang, J. Yang, B. Shi, Static liquefaction behavior of saturated fiber-reinforced sand in undrained ring-shear tests, Geotext. Geomembr. 29 (5) (2011) 462–471.
[66] R.A. Mahmood, A. Parsapajouh, A.A. Mohammad, Effects of random fiber inclusion on consolidation, hydraulic conductivity, swelling, shrinkage limit and desiccation cracking of clays, Int. J. Civ. Eng. 6 (4) (2008) 284–292.
[67] C.X. Mao, Study on piping a filters: part 1 of piping, Rock Soil Mech. 26 (2) (2005) 209–215 (in Chinese).
[68] R. Michalowski, J. Čermák, Strenght anisoropy of fiber-reinforced sand, Comput. Geotech. 29 (4) (2002) 279–299.
[69] R. Michalowski, J. Čermák, Triaxial compression of sand reinforced with fibers, *J. Geotech. Geoenviron. Eng.*, ASCE 129 (2) (2003) 125–136.
[70] V. Milligan, Some uncertainties in embankment dam engineering, *J. Geotech. Geoenviron. Eng.*, ASCE 129 (9) (2003) 785–797.
[71] M. Mirzababaei, M. Mohamed, M. Miraftab, Analysis of strip footings on fiber reinforced slopes with the aid of particle image velocimetry, *J. Mater. Civ. Eng.*, ASCE 29 (4) (2017) 04016243.
[72] R. Moffat, R.J. Fannin, Spatial and temporal progression of internal erosion in cohesionless soil, Can. Geotech. J. 48 (3) (2011) 399–412.
[73] R. Moffat, R.J. Fannin, A hydromechanical relation governing internal stability of cohesionless soil, Can. Geotech. J. 48 (3) (2011) 413–424.
[74] R.J. Nichols, R.S.J. Sparks, C.J.N. Wilson, Experimental studies of the fluidization of layered sediments and the formation of fluid escape structures, Sedimentology 41 (1994) 233–253.
[75] M. Olgun, Effects of polypropylene fiber inclusion on the strength and volume change characteristics of cement-fly ash stabilized clay soil, Geosynth. Int. 20 (4) (2013) 263–275.
[76] P.J.V. Oliveira, A.A.S. Correia, J.M.N.P.C. Teles, D.G. Custódio, Effect of fibre type on the compressive and tensile strength of a soft soil chemically stabilised, Geosynth. Int. 23 (3) (2016) 171–182.
[77] M. Parekh, W. Kanning, C. Bocovich, M.A. Mooney, A.R. Koelewijn, Backward erosion monitored by spatial-temporal pore pressure changes during field experiments, *J. Geotech. Geoenviron. Eng.*, ASCE 142 (10) (2016) 04016050.
[78] M. Peng, L.M. Zhang, Breaching parameters of landslide dams, Landslides 9 (1) (2012) 13–31.
[79] L.F.M. Pino, B.A. Baudet, The effect of the particle size distribution on the mechanics of fibre-reinforced sands under one-dimensional compression, Geotext. Geomembr. 43 (3) (2015) 250–258.
[80] M. Polemio, P. Lollino, Failure of infrastructure embankments induced by flooding and seepage: a neglected source of hazard, Nat. Hazards Earth Syst. Sci. 11 (2011) 3383–3396.
[81] G. Ranjan, R.M. Vasan, H.D. Charan, Behaviour of plastic-fiber-reinforced sand, Geotext. Geomembr. 13 (8) (1994) 555–565.
[82] J.D. Rice, J.M. Duncan, Findings of case histories on the long-term performance of seepage barriers in dams, *J. Geotech. Geoenviron. Eng.*, ASCE 136 (1) (2010) 2–15.
[83] J.D. Rice, J.M. Duncan, R.R. Davidson, Identification of failure mechanisms associated with seepage barriers in dams, *Embankment, Dams, Slope*s, ASCE (2007) 1–11.
[84] K.S. Richards, K.R. Reddy, Critical appraisal of piping phenomena in earth dams, Bull. Eng. Geol. Environ. 66 (2007) 381–402.
[85] S. Sadek, S. Najjar, F. Freiha, Shear strength of fiber-reinforced sands, *J. Geotech. Geoenviron. Eng.*, ASCE 136 (3) (2010) 490–499.
[86] S.A. Sahu, P.K. Saroj, B. Paswan, Shear waves in a heterogeneous fiber-reinforced layer over a half-space under gravity, *Int. J. Geomech.* ASCE 15 (2) (2015) 04014048.
[87] R. Santoni, J. Tingle, S. Webster, Engineering properties of sand-fiber mixtures for road construction, *J. Geotech. Geoenviron. Eng.*, ASCE 127 (3) (2001) 258–268.
[88] M.G. Sidiropoulou, K.N. Moutsopoulos, V.A. Tsihrintzis, Determination of Forchheimer equation coefficients a and b, Hydrol. Process. 21 (4) (2007) 534–554.
[89] G.L. Sivakumar Babu, A.K. Vasudevan, Seepage velocity and piping resistance of coir fiber mixed soils, *J. Irrig. Drain. Eng.*, ASCE 134 (5) (2008) 668–680.
[90] A.W. Skempton, J.M. Brogan, Experiments on piping in sandy gravels, Geotechnique 44 (3) (1994) 449–460.
[91] A.W. Skempton, J.M. Brogan, Discussion on experiments on piping in sandy gravels, Geotechnique 45 (3) (1995) 565–567.
[92] C. Tang, D. Wang, Y. Cui, B. Shi, J. Li, Tensile strength of fiber-reinforced soil, *J. Mater. Civ. Eng.* ASCE 28 (5) (2016) 04016031.
[93] C.S. Tang, B. Shi, Y.J. Cui, C. Liu, K. Gu, Desiccation cracking behavior of polypropylene fiber–reinforced clayey soil, Can. Geotech. J. 49 (9) (2012) 1088–1101.
[94] K. Terzaghi, Theoretical Soil Mechanics, Wiley, New York, 1943.
[95] V. Toufigh, C.S. Desai, H. Saadatmanesh, V. Toufigh, S. Ahmari, E. Kabiri, Constitutive modeling and testing of interface between backfill soil and fiber-reinforced polymer, *Int. J. Geomech.* ASCE 14 (3) (2014) 04014009.
[96] B.V.S. Viswanadham, S. Rajesh, P.V. Divya, J.P. Gourc, Influence of randomly distributed geofibers on the integrity of clay-based landfill covers: a centrifuge study, Geosynth. Int. 18 (5) (2011) 255–271.
[97] C.F. Wan, R. Fell, Assessing the potential of internal instability and suffusion in embankment dams and their Foundations, *J. Geotech. Geoenviron. Eng.*, ASCE 134 (3) (2008) 401–407.
[98] Y. Xu, L.M. Zhang, Breaching parameters of earth and rock fill dams, *J. Geotech. Geoenviron. Eng.*, ASCE 135 (12) (2009) 1957–1970.
[99] K.-H. Yang, W.M. Adilehou, S.-T. Jian, S.-B. Wei, Hydraulic response of fiber-reinforced sand subject to seepage, Geosynth. Int. 24 (5) (2017) 491–507.
[100] B. Ye, Z.R. Cheng, C. Liu, Y.D. Zhang, P. Lu, Liquefaction resistance of sand reinforced with randomly distributed polypropylene fibres, Geosynth. Int. 24 (6) (2017) 625–636.
[101] T. Yetimoglu, M. Inanir, O.E. Inanir, A study on bearing capacity of randomly distributed fiber reinforced sand fills overlying soft clay, Geotext. Geomembr. 23 (2) (2005) 174–183.
[102] T. Yetimoglu, O. Salbas, A study on shear strength of sands reinforced with randomly distributed discrete fibers, Geotext. Geomembr. 21 (2003) 103–110.
[103] L.M. Zhang, Q. Chen, Seepage failure mechanism of the Gouhou Rockfill Dam during reservoir water infiltration, Soils Found. 46 (5) (2006) 557–568.
[104] L.M. Zhang, Y. Xu, J.S. Jia, Analysis of earth dam failures: a database approach, Georisk 3 (3) (2009) 184–189.
[105] J. Zornberg, Discrete framework for limit equilibrium analysis of fibre-reinforced soil, Géotechnique 52 (8) (2002) 59.